

# **Hemodynamics of an end-to-side anastomosis bypass: on the specific influence of a stenosis in the host artery**

V. Deplano, C. Bertolotti.

*Laboratoire de Biomécanique Cardiovasculaire, IRPHE, UMR n°6594, CNRS, France.*

## **Abstract**

Local hemodynamics is implicated in the failure of bypass graft surgery. Intimal thickening has been shown to occur at specific sites, namely the floor, the heel, the toe and the suture line. Nevertheless, the recipient artery has often been represented in the literature as a simple flow rate reduction or as a complete obstruction neglecting the perturbing presence of the stenosis. In addition, severe as well as moderate constrictions are sometimes bypassed without taking into account an existing residual flow through the host artery. The purpose of this chapter is therefore to investigate how competitive flows issued from the graft and the diseased artery could interact together and thus to explain the restenosis process at an early stage. The velocity flow rates are issued from in vivo measurements for patients who had undergone coronary bypass surgery approximately three weeks before. 3D unsteady flows through idealized coronary bypass anastomoses are modeled by the finite element method. The influence of the inflows, and of the shape of the stenosis are notably discussed. The experimental Doppler velocity fields corroborate well the numerical results. The post-stenotic recirculation zone is demonstrated to interact with the graft inflow during the cardiac cycle. These disturbed flow patterns due to the presence of a stenosis may have harmful consequences in terms of graft patency.

## 1 Introduction

Coronary bypass surgery leads to highly traumatic operations for the patients. Within the past ten years, angioplasty and stent implantation have revealed to be a less invasive treatment for isolated lesions, whereas multiple stenoses are still surgically bypassed. In this case, to avoid reoperation, severe as well as moderate obstructions, may sometimes be bypassed without questioning about the relevance of the surgical act. Progression of atherosclerosis together with intimal hyperplasia are the most common causes of coronary bypass surgery failure. Lawrie et al. [1] give a graft patency of only 46% after 20 years of follow-up. The nature of the graft, the decision to bypass or not mild stenoses, or the mismatch between vessels diameters or compliance also remain subject to controversy [2], [3].

Otherwise, as the anastomosis thickening is confined to specific sites, specifically the floor, the heel, the toe and the suture line [4], [5], several studies emphasize the flow-induced aspects of atherogenesis [6], [7]. Local wall shear stress (wss) is demonstrated to regulate the endothelial function and thus the compensatory response in diameter of the artery [8], [9]. Oscillatory [10] and turbulent wss [11] promote endothelial proliferation. Since numerical computations remain the most convenient way to accurately characterize flows fields and wss, the recent studies tried to include additional realistic characteristics such as anatomic reconstruction of arterial segments, a non-Newtonian blood rheology, or wall elasticity [12], [13], [14]. Nevertheless, certain anatomic features may only be of a “secondary” significance with regard to the “primary” relevant phenomena induced by even simplified particular geometry or specific hemodynamics: retrograde flow, a sharp bending, a junction or a significant stenosis [15].

In fact, surgeons keep wondering about the suitability of their choices in terms of graft patency. To the author’s knowledge, the recipient artery is often represented in the literature as a simple flow rate reduction or as a complete obstruction [16], [17]. On the other hand, bypassing a non obstructed artery does not necessarily increase distal flow but rather results in flow competition [18]. The purpose of this chapter is hence to examine whether the stenosis in the host artery can significantly alter the hemodynamic patterns in the anastomosis. Emphasis is laid on the specific influence of inflow patterns, flow division between graft and host artery, severity and shape of the stenosis and finally the distance between the narrowing and the anastomosis. In vivo measurements on human coronary bypasses approximately three weeks after surgery furnish realistic inlet conditions. Numerical and experimental modeling are then performed in an idealized anastomosis whose host artery is stenosed, to bring further analysis on which primary factors influence the short or/and long-term restenosis.

## 2 Methods

This section aims to define a general methodology to simulate flow rates in coronary bypasses. In vivo measurements (§2.1) upon bypassed patients serve as basis in the model constitution. The numerical computations (§2.2) are completed and validated with in vitro experiments (§2.3).

### 2.1 In vivo measurements

Following our indications, a cardiologist performed velocity measurements upon two recently operated patients. When technically possible by means of intravascular Doppler catheter (Cardiometrics), velocity measurements are recorded at several locations into the multiple bypasses. This minimally invasive technique is mainly limited by the uncertainty in positioning the catheter into the artery lumen but also by flow impairment due to the invasive procedure. The resistance to flow is supposed to double with such catheter-to-artery diameters ratio [19]. Despite these known limitations, the approach has been validated by Doucette [20] and was the only way to get local instantaneous velocity information. The local ethic committee approved the experiment and all the patients gave their informed consent before the study.

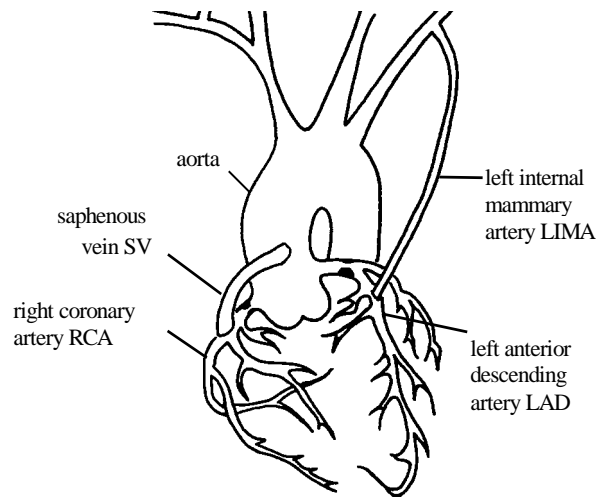


Figure 1: Schematic representation of coronary bypass surgeries.

The examined patients underwent a triple coronary bypass grafting between one to three weeks before. The surgical act can include one or more of the following configurations (Figure 1):

- left internal mammary artery LIMA on left anterior descending coronary LAD (this case is designated by PH1 in the present study),
- saphenous vein graft SV on left diagonal artery LAD,
- SV graft or right internal mammary artery RIMA on right coronary artery RCA (the case with SV graft is called PH2).

Simultaneous radioscopic images help to localize the 0.014-inch guide inside the vascular anastomosis. The gradual adaptation of flow phase observed by Bach [21] along the graft has been confirmed here since flows are diastolic within the two grafts, a few diameters upstream from the anastomosis. In contrast, the residual flow of the host artery can either be diastolic, showing the influence of myocardial contraction, or systolic. Actually, PH2 (Figure 2) reveals a non-negligible systolic component that can be due to both the very short artery length (less than 10 diameters long in this patient) and to the weaker contraction of the right myocardium (already noticed by Berne & Levy [22]).

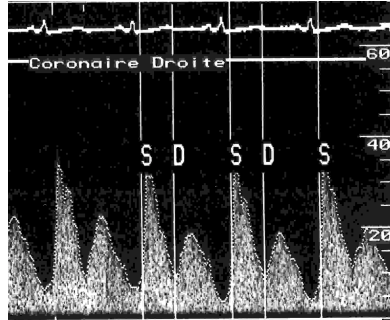


Figure 2 : Example of in vivo recorded velocity into RCA (PH2 case: SV grafted onto RCA).

As the catheter is supposed to rest at the vessel center, the flow rate  $Q_{\phi}(t)$  is estimated from the measurement of the axial velocity  $V_{\phi_{max}}$  and from the radii  $R_{\phi_0}$  of native arteries (e.g. varying from 1.35 to 2.1mm for the SV):

$$Q_{\phi}(t) = 1/2 \pi R_{\phi_0}^2 V_{\phi_{max}}(t) \quad (1)$$

In rigid cylinder, this approximation is valid for parabolic profiles at low Reynolds numbers  $Re_{max}$  and laminar flow i.e. for low Womersley parameter

$\alpha = \sqrt{\omega_\phi / \nu_\phi} R_{\phi 0}$ , where  $\nu$  represents the kinematic viscosity and  $\omega$ , the cardiac frequency [23]. Since  $\alpha \approx 2.2$  in all cases and as the inlet velocity is implemented upstream from the stenosis, this assumption seems justified. After Fourier decomposition of these time-varying approximated flow rates, reconstructed velocity profiles are implemented to inlet boundary conditions of numerical computations and experiments.

## 2.2 Numerical computations

All numerical computations are carried out by means of finite elements methods (N3S package, [24]). Preliminary tests under steady flows [25] allow to optimize mesh strategy and to achieve convergence.

### 2.2.1 Physical model

**2.2.1.1 Geometry** The anastomosis (Figure 3) is defined as the 3D analytical intersection of two cylinders of an equal diameter  $D_\phi = 3$  mm, with a  $45^\circ$  junction angle. Two typical stenosis shapes are modeled. The axi-symmetric stenosis (75%- or 84%-area severity) is longitudinally described by a Gaussian profile:

$$R_\phi(x) = R_{\phi 0} \left( 1 - p \exp\left(\frac{-4x^2}{R_{\phi 0}^2}\right) \right) \quad (2)$$

where the radius of the constricted tube  $R_\phi$  is a function of axial position  $x$ ,  $R_{\phi 0}$  is the radius of the unstenosed tube ( $R_{\phi 0}=1.5$ mm) and  $p$  varies with stenosis severity ( $p=1/2$  for a 75% stenosis and  $p=3/5$  for a 84% one). The stenosis can be located at  $2D_\phi$  or  $3D_\phi$  upstream from the heel. The second shape is a 75% eccentric narrowing whose lumen is a cut disc. The narrowing is placed at the bottom wall and its longitudinal profile is also Gaussian. The origin  $(O,x,y,z)$  of the Cartesian coordinates system is the intersection of the axes of each tube.

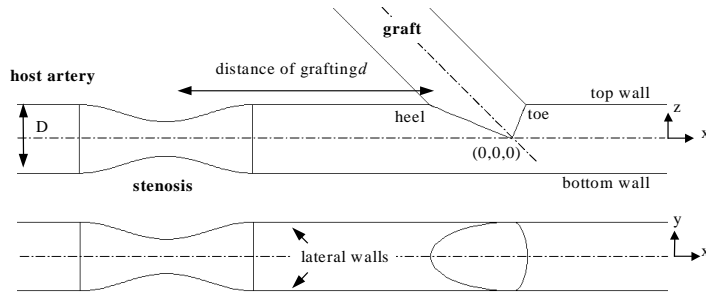


Figure 3: Geometry of the coronary bypass model.

**2.2.1.2 Assumptions** Several authors have discussed about the laminarity of flow through stenosis. Their experimental measurements pointed out that above critical Reynolds numbers between 300 and 400, the flow can become transitional and turbulent in presence of similar 75% severity stenosis and shape [26], [27], [28]. Hence the model is chosen laminar as the highest mean Reynolds is only of 170 (Table 1).

The following hypotheses are:

- the walls are rigid and non-porous,
- the flow is unsteady, three-dimensional and laminar,
- the fluid is incompressible, Newtonian, viscous, and isothermal.

**2.2.1.3 Similitude** Problems of precision, both in mesh realization and in experimental conditions convey to enlarge the geometric scale by a factor 2. If suffix  $\phi$  indicates the physiological reality (no suffix designating our model), the use of similitude implies to increase respectively diameter, cardiac period and kinematic viscosity:  $D=2D_\phi$ ,  $T=2T_\phi$ ,  $\nu=2\nu_\phi$ . So that with respect to Reynolds number  $Re$  and Womersley parameter  $\alpha$ , the velocity is unchanged and the modeled flow rate becomes:  $Q(t)=4Q_\phi(t)$ .

### 2.2.2 Mathematical model

The three-dimensional unsteady flow is governed by the Navier-Stokes equations. Considering the previous hypotheses, the equations to be solved can be formulated in the Cartesian co-ordinates reference frame as:

$$\frac{\partial \vec{v}}{\partial t} + \vec{v} \overline{\text{grad}} \vec{v} + \frac{1}{\rho} \overline{\text{grad}} p - \nu \Delta \vec{v} = 0 \quad (3)$$

$$\text{div} \vec{v} = 0 \quad (4)$$

where  $\vec{v}$  is the velocity vector,  $u$  being the velocity component in the  $x$  direction,  $v$  and  $w$  are those in  $y$  and  $z$  ones,  $t$  is the time,  $p$  is the pressure. The kinematic viscosity  $\nu$  is the same as blood, i.e.  $\nu_\phi = 3.6 \cdot 10^{-6} \text{ m}^2 / \text{s}$ , and the density is approximated to  $\rho = 1000 \text{ kg} / \text{m}^3$ .

### 2.2.3 Boundary conditions

- Along the walls, we apply the usual no-slip velocity specifications:

$$u = v = w = 0. \quad (5)$$

- At the inlet, radial and tangential components of the velocity are zero. Three types of unsteady flow rates are imposed (Figure 4): in vivo flow rates (namely PH1 and PH2 previously described in §2.1) and Berne & Levy flow BL [22] which is the only human coronary flow rate found throughout literature. First flow rates are implemented as encountered in vivo. Latter conditions are applied with different graft to artery ratio of the outlet flow  $Q(t)$  (see the recapitulative Table 3, §3.2). Whatever the case, Womersley parameter is about 2.2. The occluded case, BLO, represents an occluded host artery.

Table 1: Recapitulative table of inlet boundary conditions.

Referred by case	Host artery		Graft	
	Re	Re <sub>max</sub>	Re	Re <sub>max</sub>
PH1	72.3	113.1	131.3	270
PH2	86	162.7	147.4	295
BLO	48.5	97.4	48.5	97.4

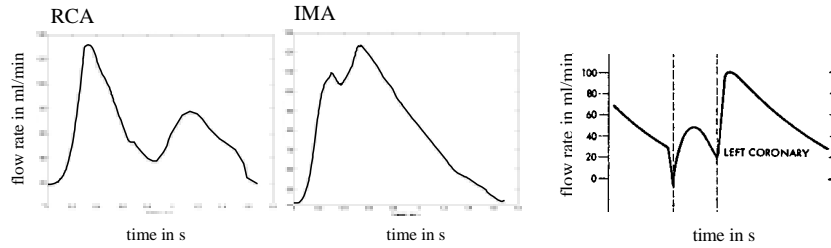


Figure 4: Imposed flow rates : PH2, PH1 and BL.

- At the outlet, no stress conditions are imposed. This yields:

$$-p + \frac{1}{Re} \frac{\partial u_n}{\partial n} = 0 \quad (6)$$

where  $u_n$  is the normal component of  $\vec{v}$  and  $\vec{n}$  the unitary normal vector at the outlet section.

#### 2.2.4 Numerical algorithms

The set of equations (3) and (4) is non-linear and time dependent. The variational formulation of the problem leads to a spatial discretization of equations based on Lagrange finite element method (N3S Package [24]). The computational domain

is broken up into tetrahedral elements of type P1-isoP2 where the approximation is quadratic for the velocity and linear for the pressure. The time is discretized using a fractional step scheme of order 2. A provisional value for velocity is computed for the convection step by means of the characteristic method; the diffusion or Stokes step is computed from an implicit Euler scheme: the Chorin algorithm [29]. The linear system is finally solved using the conjugate gradient method. The time convergence test is based on the calculation of the residu for three different norms:  $L_1$ ,  $L_2$  and  $L_\infty$ .

In our simulations, periodic steady state solutions of the Navier-Stokes equations are reached at the second period with an error within 0.6% compared to the third period. With a time step of  $2.5 \cdot 10^{-4}$  s and 6400 iterations, the CPU computation time is of 48h for one period (Origin 200, Silicon Graphics, 4-processors R1000, 512MB). Therefore, the reported results are those obtained at the second period.

### **2.2.5 Meshes**

A sufficient development length in the longitudinal direction is needed to avoid the hypothetical perturbations of the outlet boundary conditions: accordingly, the computational domain extends from  $x=-3.72\text{cm}$  to  $x=5.94\text{cm}$ . Preliminary tests have been performed upon single stenosed tube. Spatial mesh refinement has been carried out until post-stenotic jet flow becomes axisymmetric and mesh-independent. For example, one of the final meshes is constituted by 17693 P1 nodes for the pressure discretization and 129356 P2 nodes for the velocity discretization. It is refined from the inlet to the stenosis, from the outlet to stenosis along x-axis direction and also in the radial direction, from the x-axis to the wall.

## **2.3 Experimental set up**

A custom-built experimental bench allows to generate low flow rates as encountered in coronary arteries. Ultrasonic velocity measurements have been performed in coronary bypass molds.

### **2.3.1 Test bench**

The test bench (Figure 5) is a modular mock flow circulation comprising two volumetric pumps, the vascular test section, a distal resistance represented by a collector tank. The gear pumps are computer-controlled throughout Labview (ATMIO16E-10 card, National Instruments) in order to generate physiological waveforms as well as any kind of cardiac frequency, flow shape and magnitude. This type of hydrodynamic generator was not adapted to such low flow rates (100-300ml/min) so that flow oscillations synchronised with gearwheels rotation

have been observed. The width of the gear have been specifically reduced so that gear rotation speed is increased to produce the same flow rate. Thus perturbations become negligible. Flow rates are recorded with two electromagnetic flowmeters Gould Statham SP2202 whose accuracy is within 10%. To mimic blood viscosity, the working fluid is a mixture of 27%-demineralized water and 73%-polyethylen-glycol (Napel 2050, British Petroleum). At 22°C, the dynamic viscosity  $\mu$  of this fluid is of 7.2cP according to the similitude (Couette rheometer, Rheovisco ELV-8).

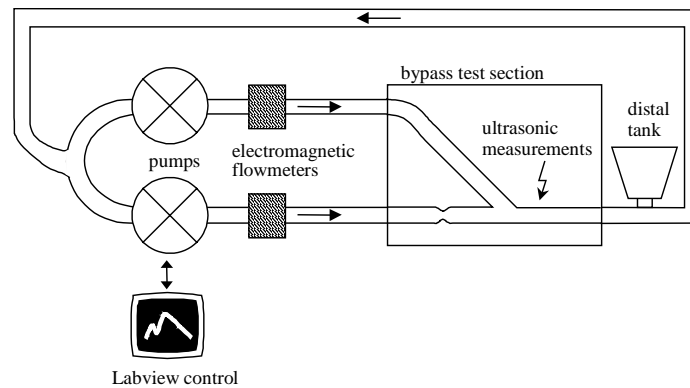


Figure 5: Modular mock flow loop.

### 2.3.2 Bypass test section

**2.3.2.1 Set up** The bypass cast is micro-mechanically machined in two brass rods whose surfaces are polished to facilitate removal of the mold. Once the graft rod is fixed at the entrance, the stenosed rod can slide between the connectors in order to accurately adjust the stenosis position with a gauge. These specific dug connectors are also machined to permit the molding of integrated flanges at the ends. Three metal stirrups screwed onto a metal slab, maintain the cast and the connectors in bypass geometric configuration. After molding procedure (see §2.3.2.2), the whole setting is dismantled from the metal slab, to be screwed again onto a Plexiglas disc in the same geometric configuration (Figure 6). To limit the bending of the bypass, the silicon mold is tensioned between the stirrups thanks to the flanges and the Plexiglas disc is hold vertically. A last optical micro-control (Smartscope, accuracy  $\pm 5\mu\text{m}$ ) enables to check the geometric location of the anastomosis center.

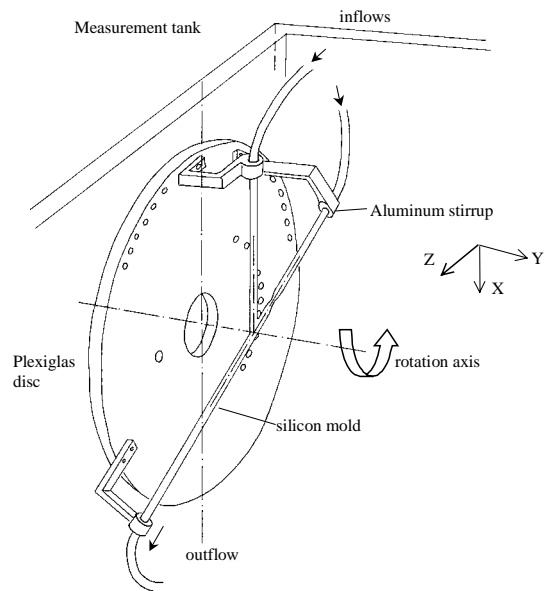


Figure 6 : Test section.

**2.3.2.2 Silicon moulding procedure** The mold is fabricated following a step-by-step dipping method. First, the whole metal setting described in §2.3.2.1 is plunged into a degased clear silicon rubber dissolved with white spirit at concentration of approximately three parts solvent to one part Silopren LSR 2050 (Bayer Silicons). The dipped cast is then placed on a rotary arm for 30 minutes to homogenize the thickness of the layer, and cooked at 200°C. Such operations are repeated until desired wall thickness is obtained (between 0.3mm and 0.6mm). After cooling, the silicon mold (Figure 7) can be removed from the metal cast and positioned onto the Plexiglas disk. Compliance  $C_0$  and relative pulsatility  $Pr$  of the silicon tubes have been estimated under pulsatile conditions on a specific test bench: external diameter and flow pressure were measured at the same site, respectively with a sonomicrometer (Triton Technology, San Diego, USA) and a Mikro-Tip catheter (Millar MPC-500, 5F). Viscoelastic properties were found close to those of native arteries (Table 2).

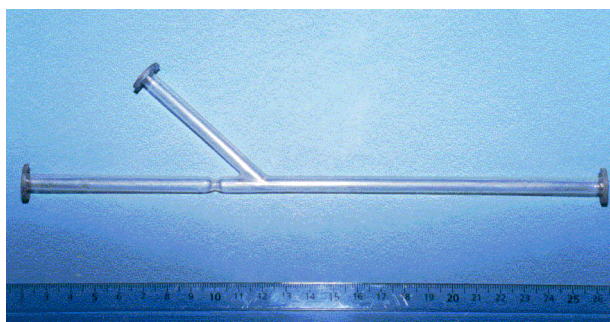


Figure 7 : Bypass silicon mold.

Table 2: Comparison of rheological properties of a native iliac artery and our silicon mold.  $Co = \Delta V / \Delta P$  where  $\Delta V = V_{max} - V_{min}$ , is the variation of the arterial volume and  $\Delta P = P_{max} - P_{min}$ , is the differential pressure.  $Pr = \Delta D / D_{mean}$  where  $\Delta D = D_{max} - D_{min}$  is the maximal variation of external diameter during the cardiac cycle and  $D_{mean}$  is the mean diameter.

Rheologic parameters	Iliac artery	Silicon mold
Co (ml/mmHg)	$7.67 \cdot 10^{-04}$	$6.53 \cdot 10^{-04}$
Pr (%)	3.41	4.98

### 2.3.3 Doppler velocity measurements

Velocity measurements are performed using a multichannel 8MHz-pulsed Doppler velocimeter (Dop1000, Signal Processings, Switzerland). With a burst length of 4 pulses, the longitudinal resolution is of 0.425mm giving a sample volume of about  $0.12\text{mm}^3$ . Superfine starch particles act as ultrasound scatterers. The whole test section is immersed in a bath of the same fluid to ensure coupling with the transducer but also to limit possible refraction effects at the different interfaces. The ultrasonic wave celerity was found of  $1700 \pm 28\text{m/s}$  in the working fluid (test was performed by Signal Processings). The probe-holder is designed to impose an incidence angle of  $\beta = 23.8^\circ$ . By means of high precision rulers, the probe can be moved to x-y-z position and around x-axis with a displacement resolution of 0.01mm. Velocity measurements are performed in two planes: the symmetry plane xOz and its orthogonal plane xOy. The flow field is reconstructed from the two velocity components collected at  $+\beta$  and  $-\beta$  in each plane. All the sections (Figure 8) are covered by 572 displacements. Finally, instantaneous velocities are averaged over 30 cardiac periods to ensure reproducibility.

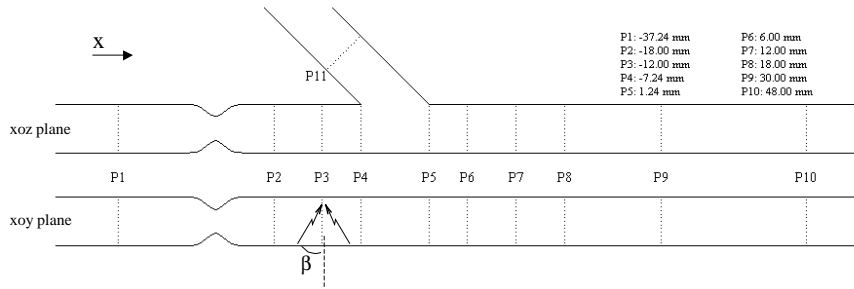


Figure 8: Experimental velocity meshes.

### 3 Results

Since post-stenotic flows patterns, as well as junction flows, have been widely investigated throughout literature, general phenomena associated with each configuration are shortly presented in section (§3.1). In the following of this chapter, we rather concentrate on their interaction. Table 3 and Table 4 display all the studied cases. Section §2 presents the hemodynamics of a stenosed bypass with a special emphasis on the influence of nature of the two inflows (§3.2.1), the shape of the stenosis (§3.2.2), and finally the distance of grafting (§3.2.2.2). Last results deal with local analysis of the wall shear stress (wss) into different bypass configurations (§3.3).

#### 3.1 General phenomena associated with junction flows and with post-stenotic flows

##### 3.1.1 Junction flows

Flow phenomena occurring in junction geometry are similar to those generally observed in curved pipes. The change in main flow direction causes the onset of imbalance between centrifugal forces and transverse pressure gradient. In our anastomosis model, particles located at the center of the graft are submitted to centrifugal forces when graft flow penetrates host artery flow. The axial velocity peak of the host artery is pushed towards the bottom wall of the junction. Conversely, at the top wall, opposite movements originate from the pressure gradient. Accordingly the classical counter-rotating vortices are generated in the cross-sectional plane to the longitudinal axis (see Figure 9). They usually develop between top and bottom walls initially close to the lateral walls. Their core moves towards the center axis further downstream. These two helical structures longitudinally grow relative to the symmetry plane of the anastomosis, namely xOz

plane (see Figure 3). A few diameters downstream from the junction, the three-dimensional effect dissipates and the velocity maximum retrieves its axially-centred position in the host artery. Many authors reported that the strength of secondary motions increases with angle of grafting and with Reynolds number in the graft [30], [31], [32], [33], [34]. Moreover, a stasis zone can develop at the toe of the anastomosis. Its longitudinal extension increases in the same manner as secondary patterns so that surgeons encourage to bypass with a minimal angle. In the presented results, the angle of grafting is  $45^\circ$  and the BLO case serves as reference of a simple junction flow with an occluded host artery.

### **3.1.2 Post-stenotic flows**

Typical velocity profiles emerge downstream from a local constriction. In our model, the residual flow issued from the stenosed host artery creates a confined jet, with a potential core bounded by the shear layer zone which links up to the wall by a recirculating area.

Depending on the time in the cycle and on the longitudinal distance downstream from the throat, the pulsatile wake generates different profile shapes, evolving from flat-shaped to conical-shaped. The velocity acceleration due to the geometrical constriction leads to flat-shaped profiles with a very thin boundary layer at the stenosis throat. Then, fan-shaped profiles can occur in the closer vicinity downstream from the stenosis. They are representative of strong radial velocities superimposed on parabolic longitudinal velocity profiles. These profile shapes are noticeable during the acceleration part of the cycle (see  $t=0.16s$ , Figure 9). Top hat shaped profiles are observed at the stenosis outlet (see Figure 12). The constant velocity values in the central part correspond to the potential core of the jet coming from the throat. The negative velocity values at the walls obviously originate in the recirculating area.

More downstream, where potential core ended, flat profiles become rounded as bell-shape with still negative velocity values at the walls (see Figure 12).

Finally, conical shaped profile are observed near the reattachment region of the stenotic jet (see  $t=0.56s$ , Figure 21). Such characteristic shapes have also been observed by [35], [36].

## **3.2 Influence of a stenosis in the host artery upon hemodynamics in the anastomosis : numerical results**

The two following tables (Table 3 and Table 4) list the results referred by case.

Table 3: Recapitulative table of grat to artery flow division cases with Berne & Levy outlet flow rate of Q.

<b>Flow division (graft:host artery)</b>	Q/2:Q/2	3Q/4:Q/4	Q:-
<b>Case</b>	BL12	BL34	BLO

Table 4: Recapitulative table of the different simulated cases with physiological flow rates PH1 and PH2.

<b>Severity</b>	75%			84%
<b>Shape</b>	concentric		eccentric	concentric
<b>Distance of grafting</b>	2D	3D	2D	2D
<b>PH1</b>	2D-75PH1	-	-	-
<b>PH2</b>	2D-75PH2	3D-75PH2	2D-ec75PH2	2D-84PH2

### 3.2.1 Residual flow into the host artery

The existence of a residual flow in the recipient artery is quite common especially when multiple bypass grafts are carried out in the same time. Mild stenoses of less than 75% are often grafted as well as the more severe ones.

**3.2.1.1 Graft-to-artery flow division** The goal of this section is to analyze whether flow division between host artery and graft has a determinant influence on the hemodynamic patterns in coronary bypass anastomosis.

Longitudinal velocity profiles (Figure 9) are plotted along xOz and xOy planes as represented in Figure 3. The longitudinal velocity vectors reveal the expected recirculating area downstream from the stenosis. Under pulsatile conditions and whatever the flow division BL12 or BL34, this area grows, decreases and oscillates during the cycle. The recirculation area begins to elongate during systole at the first flow deceleration. It plainly develops, sometimes up to the heel during the diastole and till the middle of second deceleration. Of course, the greater the residual flow, the more marked is the growth of the recirculation (BL12, Figure 9).

Using the dimensionless form of the transport equation of the rotational, Siouffi et al. [35] have pointed out that the extent of recirculating area is linked to the value of  $Re_{max}$ . The extension term of the vortex lines as well as rotational convection term are proportional to  $Re_{max}$ . The downstream propagation of the recirculating area is thus facilitated by high peak flow through stenosis as BL12

case demonstrated. In addition, owing to the transport time of the rotational, the maximal longitudinal and radial expansion of the recirculation is reached during the diastolic deceleration. The secondary motions in cross-sectional planes (Figure 10) also announce the propagation of the vortex ring. Indeed, a “star structure” forms, especially visible on BL34 at  $x/D=-2.2$ , during the acceleration phases. This structure indicates the presence of radial velocities directed from the center to lateral walls, following preferential directions.

Without any residual flow into the recipient artery (BLO case), flow patterns are radically different in the proximal segment. During acceleration phase, the particles get such an important inertia that the graft flow is completely directed towards the distal segment (Figure 11). On the other hand a retrograde flow is initiated towards obstruction at early deceleration and evolves along bottom wall, just upstream from the junction. This vortex occupies the whole section of the obstructed artery until the end of diastole. Obviously this phenomenon does not exist as soon as residual flow passes through the stenosed host artery.

Downstream from the junction, several studies have detected the existence of dead fluid at the toe. For the BL34 case, the stasis zone extends to 1D upstream from the toe. Its extension is maximum (2D downstream from the toe) for the occluded case, whereas missing for the BL12 case. These results clearly show that the stenosis influence propagates downstream from the junction. Jet flow noticeable in BL12 longitudinal profiles, forces the fluid reattachment at the toe. Finally, while occupying the whole section in simple junction flow BLO, the structures are confined in the top half cross-section because of the jet strength (see Figure 10).

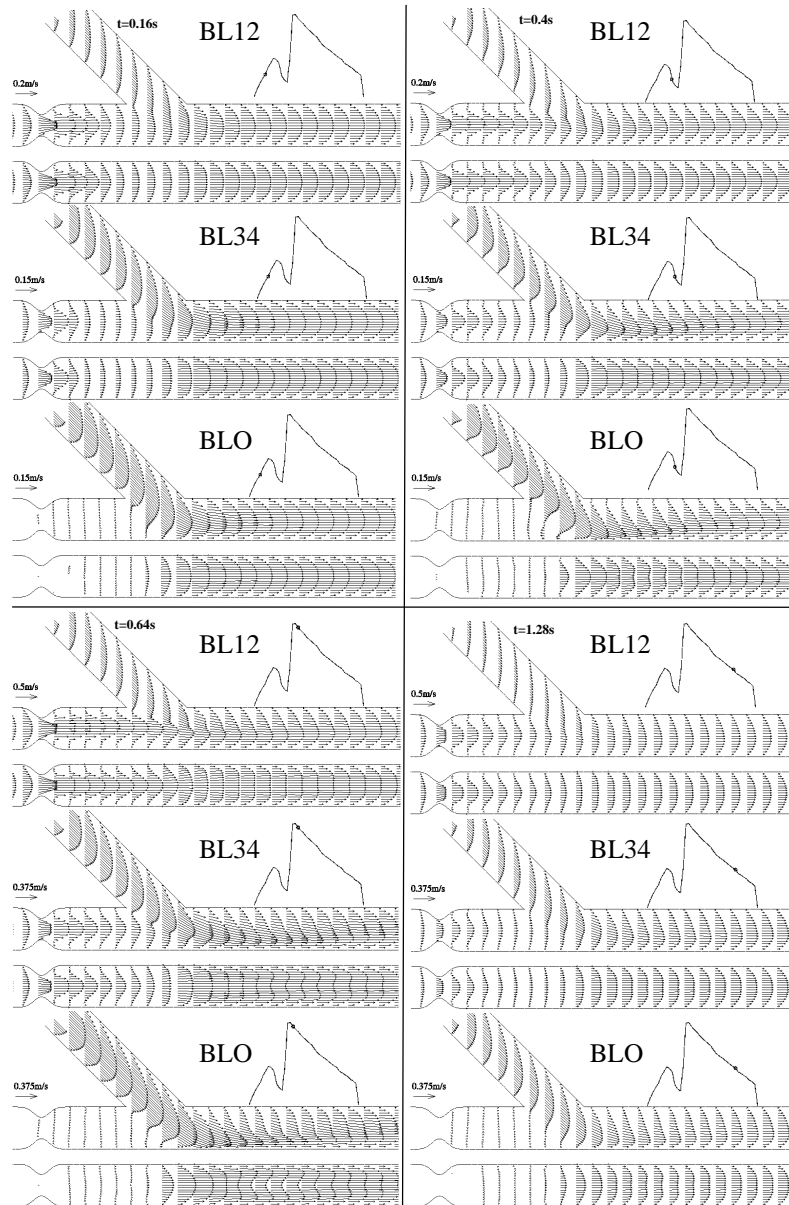


Figure 9: Longitudinal velocity profiles for BLO, BL12, BL34 and four times along the cycle:  $t=0.16s$ ,  $t=0.4s$ ,  $t=0.64s$  and  $t=1.28s$ .

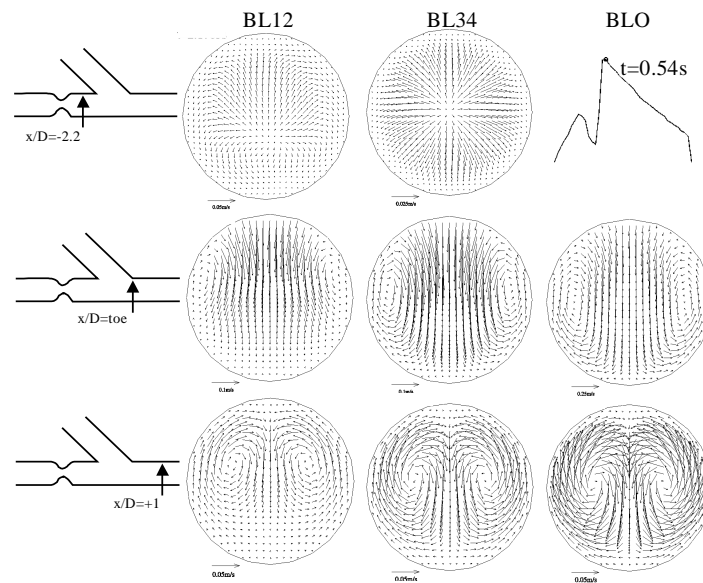


Figure 10: Secondary vortices at  $t=0.54s$  for BL12, BL34 and BLO.

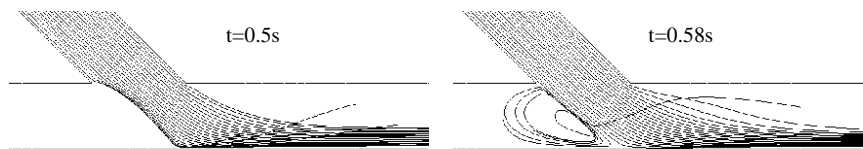


Figure 11: Emission-lines for BLO, the occluded host artery case.

**3.2.1.2 Dephased inflows** The results (longitudinal velocities: Figure 12, emission-lines: Figure 13 and secondary motions: Figure 14) are presented to analyze the influence of inflow out of phase.

The phase difference in 2D-75PH2 seems to intensify the longitudinal and radial extension of the influence length. The post-stenotic influence length is more extended in 2D-75PH2 than 2D-75PH1, confirming also the dependence on  $Re_{max}$  previously discussed in §3.2.1.1. With two diastolic inflows (2D-75PH1) a minor jet deflection towards the top wall is observed at maximal stenosis flow rate in the host recipient artery.

On the contrary, with mismatching inflows, that is, diastolic flow through the graft versus systolic flow into the recipient artery, the recirculation develops in a non-symmetrical manner. While the graft flow decelerates in early systole, the post-stenotic jet deflection towards the bottom wall lasts until  $t=0.32s$ .

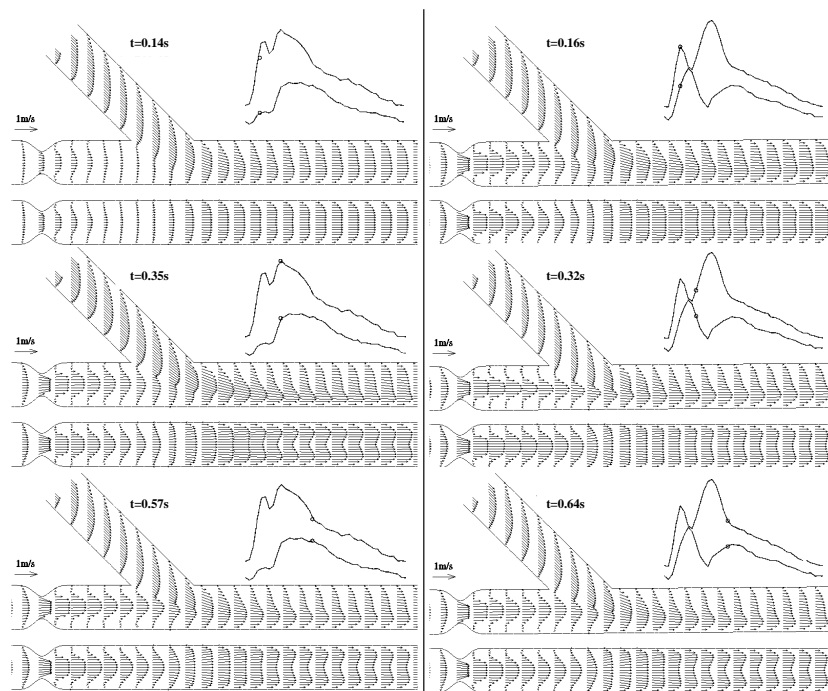


Figure 12: Longitudinal velocity profiles for physiological cases PH1 et PH2.

The emission-lines (Figure 13) clearly highlight that, synchronized with the beginning of acceleration into the graft, a few particles issued from the graft, manage to go back, supplying the formation of the recirculating vortex at the heel. As graft flow accelerates, this feedback phenomenon is amplified benefiting from the weakening of the jet.

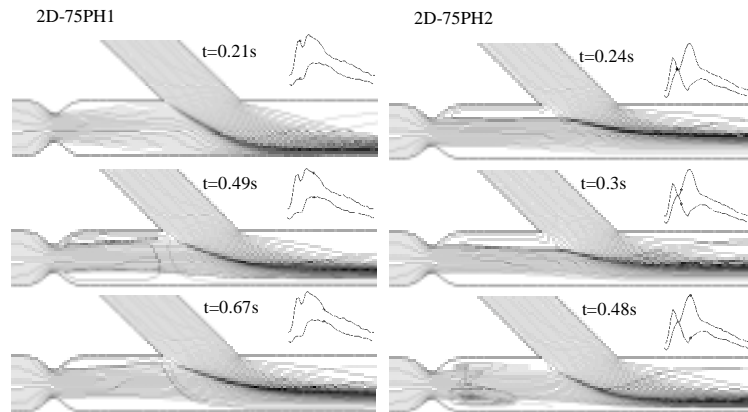


Figure 13: Emission-lines in the physiological cases 2D-75PH1 et 2D-75PH2.

During this critical period, secondary motions at  $x/D=-2.2$  become asymmetric relative to the symmetry plane (Figure 14). Later in the cycle, cross-sectional planes show non-negligible  $v$  and  $w$  components of the velocity: a large area of disturbed recirculating flow grows at the top wall in systole and, from late systole to the cycle end, at the bottom wall. As reported several authors [37], [38], small perturbations are observed at the first stage in the axial velocities leading to slight deformation of the vortex ring. If  $Re$  increases, the post-stenotic jet can periodically flap even with steady inflow. These non-symmetrical patterns may also be due to the particles feedback. This occurrence is specifically noticeable in 2D-75PH2 whereas 2D-75PH1 case is less disorganized.

Downstream from the junction, we observe that, for a stronger jet influence (2D-75PH2), the counter-rotating vortices remain confined as already noticed with BL12.

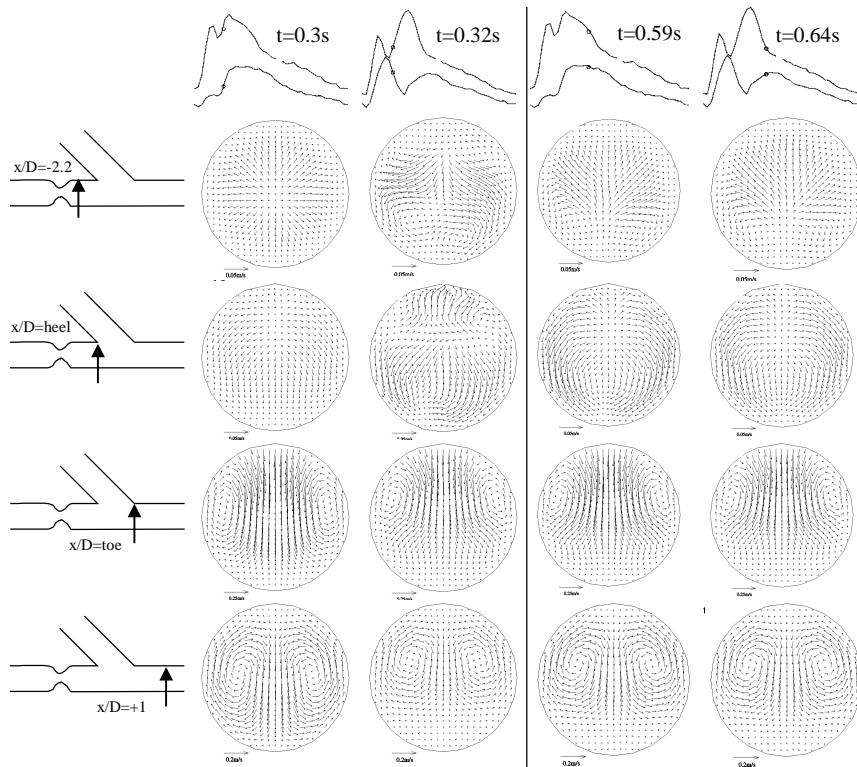


Figure 14: Secondary motions in  $yOz$  planes for 2D-75PH1 et 2D-75PH2 during systole (left) and diastole (right).

### 3.2.2 Influence of the stenosis shape

**3.2.2.1 Severity** Major myocardium ischemia are often due to high grade stenoses. We compare here the previous 75% stenosis case 2D-75PH2 with a more severe axi-symmetric stenosis of 84% for the same PH2 inflow.

The outstanding phenomenon observed in 2D-84PH2 is a major deflection of the post-stenotic jet towards the top wall and one of the lateral walls. Accordingly an asymmetrical recirculating area is observed downstream from the 2D-84PH2 stenosis, more intensive and more radially extended than the 2D-75PH2 case (Figure 15). As described in §3.2.1.1 this phenomenon is more marked at the beginning of the systolic deceleration of the host artery flow.

Due to the major jet deflection towards the top wall, the maximum of the longitudinal velocity in the  $xOz$  planes, classically observed towards the bottom wall

distal to the junction, is located more centrally for the 2D-84PH2 (Figure 15  $t=0.32s$ ). In addition, the  $xOy$  planes highlight the existence, downstream from the junction, of a longitudinal velocity distortion towards the top wall according to the lateral jet deflection. As the reattachment point of the recirculation region distal to most severe occlusion moves further downstream ([39]) the reattachment point in the 2D-84PH2 case, unlike the 2D-75PH2 case, does never reattach whatever the time.

The emission-lines (Figure 16) highlight that, unlike 2D-75PH2, the strong deflected jet towards the top wall prevent the graft flow from going back into the recirculating area. On the other hand, a few of these particles go into the recirculating area located at the bottom wall (see  $t=0.24s$ ,  $t=0.32s$ ).

The secondary structures observed for the 2D-84PH2 case at  $x/D=+1$  downstream from the junction (Figure 17), in planes perpendicular to the main flow, present strong differences in relation to the 2D-75PH2 case. Until the graft flow rate accelerates ( $t=0.16s$ ,  $t=0.4s$ ) we observe approximately the same phenomenon for both cases with the classical counter-rotating vortices, more or less extended in the whole cross section depending to the jet influence. As the host artery flow rate reaches its maximum and begins to decelerate ( $t=0.24s$ ,  $t=0.32s$ ) we notice the onset of two others non symmetrical vortices in the lower part of the cross section. These phenomena can be correlated with those occurring in the vertebro-basilar junction (see [39], [40]). In that native confluence, the two inflows merge into the host artery with a certain angle, initiating four counter-rotating secondary vortices downstream from the junction. In our case, the first change in flow direction is imputable, unlike the confluence, to hydrodynamic: the jet deflection towards one side between the top and one lateral walls. Then, the inflow issued from the graft branch superimposes a second change in geometrical axis direction. Four counter-rotating structures are thus generated. The two ones coming from the jet deflection are weaker than the two others, again like in confluence with a non uniform flows repartition. In addition, since the directions of both jet and graft inflow are not symmetric relative to the symmetry plane of the anastomosis, a distortion can be observed in the additional counter-rotating vortices. As a consequence, from the two secondary structures generated downstream from the stenosis, only one is prevalent at the bottom wall (see  $t=0.24s$  and  $t=0.32s$  in Figure 17

At  $x/D=heel$ , as the host artery flow rate reaches its maximum and begins to decelerate ( $t=0.24s$ ,  $t=0.32s$ ), the flow issued from the graft rolls up asymmetrically along the lateral walls on both sides of the top wall recirculating area. The lateral jet deflection stops one of the rolling up creating a first vortex. The interaction between the two lateral rolling up implies the onset of two additional counter-rotating vortices.

More upstream, at  $x/D=-2.2$ , complex asymmetric secondary structures issued from the disorganization of the vortex ring are observed.

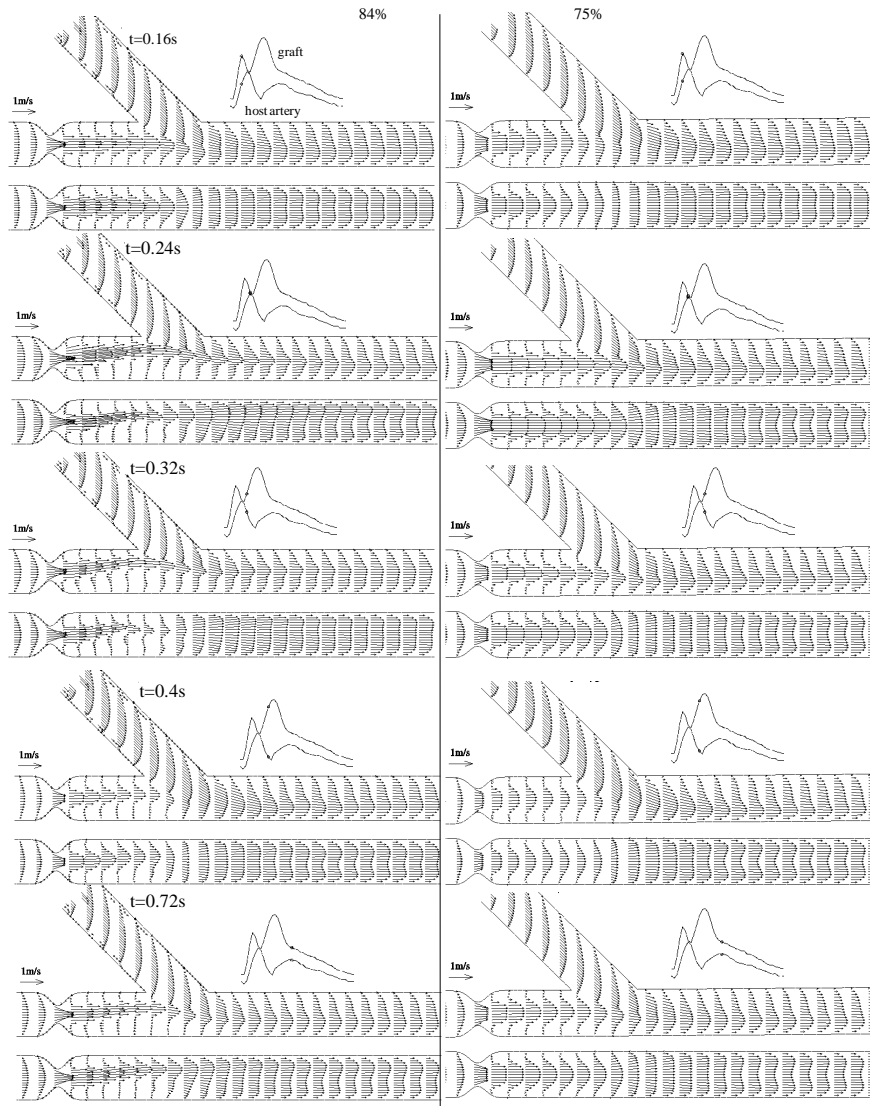


Figure 15: Longitudinal velocity profiles for a 84% concentric stenosis 2D-84PH2 (left) versus a 75% stenosis 2D-75PH2(right).

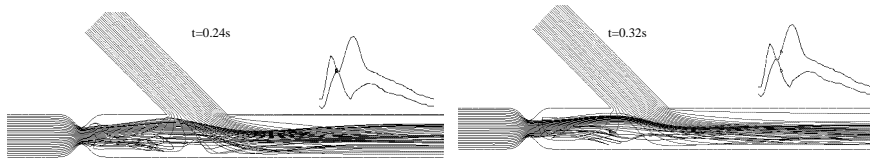


Figure 16: Emission-lines for 2D-84PH2.

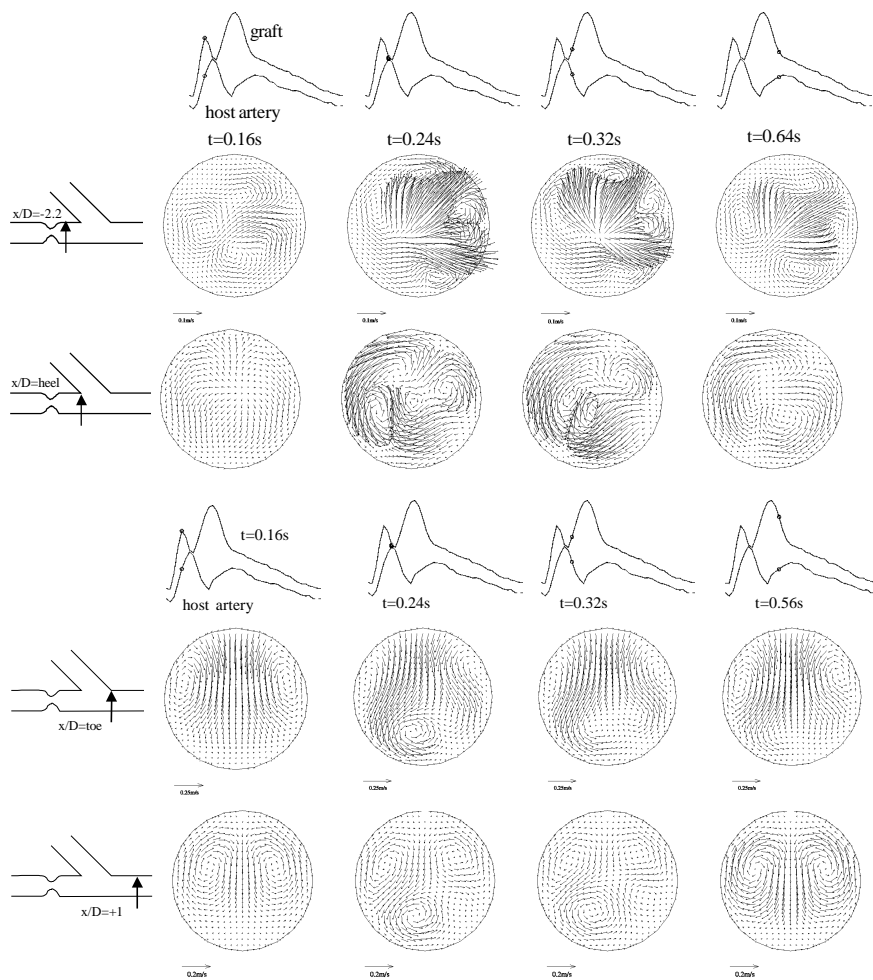


Figure 17: Secondary motions in  $yOz$  for a 84% stenosis (2D-84PH2).

**3.2.2.2 Eccentricity** A post-mortem study has recently revealed that the maximal fibromuscular intimal thickening is preferentially found on the myocardial side in case of proximal RCA [42]. 51% of the samples appeared to be sites of eccentric intimal growth. The 2D-ec75PH2 case representing one of these typical in vivo stenosis shape, we compare the flow patterns for an eccentric versus concentric lesion of the same 75% severity, same length and same distance of grafting (longitudinal velocities: Figure 18, emission-lines: Figure 19, secondary motions: Figure 20).

The flow patterns are significantly different as, during the major part of the cycle, the flow through the stenosis throat is pushed inwards the anastomosis along the top wall. The intensity of this "penetration" follows that one of the host artery flow rate. In the  $xOy$  planes the back flow at the top wall is thus absent, unlike 2D-75PH2 case : the whole recirculation is no more circumferential. In addition, the recirculating area at the bottom wall is obviously radially and longitudinally more extended than the axi-symmetric 75% stenosis case. Low back flow can also be seen at the lateral walls, according to the  $xOz$  planes, once again this recirculating area is more radially and longitudinally extended than the 2D-75PH2 case. Furthermore a few particles of the bottom recirculation go back upstream to the stenosis (see  $t=0.24s$ ,  $t=0.32s$ , Figure 20) creating a small recirculating area upstream the narrowing. This non circumferential recirculating area particularly radially extended at the bottom wall is more highlighted by the secondary structures at  $x/D=-2.2$  with a large ascending motion from the bottom wall to the cross sectional centre. We can also notice on these planes the strong amplitude of the radial velocities. At  $x/D=heel$  the flow issued from the graft do not manage at all to pass through the strong jet along the top wall and they just reinforces each others. The secondary structures are thus very similar to those observed at  $x/D=-2.2$  with a lower and less extended recirculating area at the bottom wall and more intensive radial velocity values. From the toe location, the secondary structures do not present important differences with the 2D-75PH2 case.

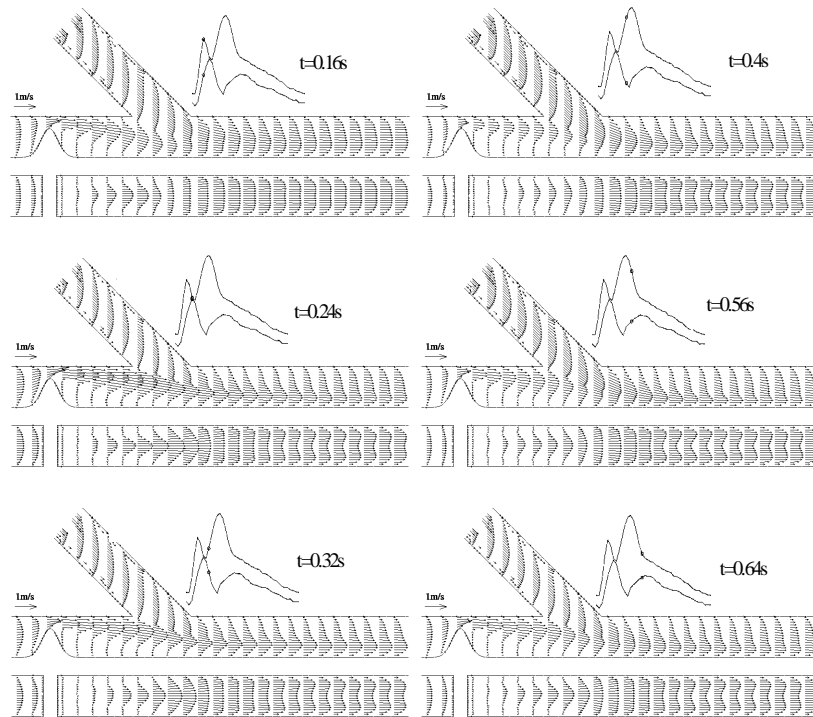


Figure 18: Longitudinal velocity profiles for the 2D-ec75PH2 case

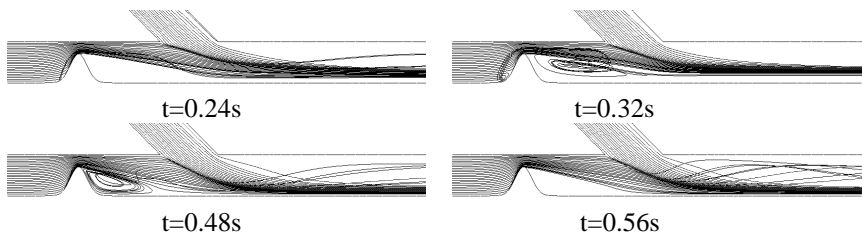


Figure 19: Emission-lines for 2D-ec75PH2.

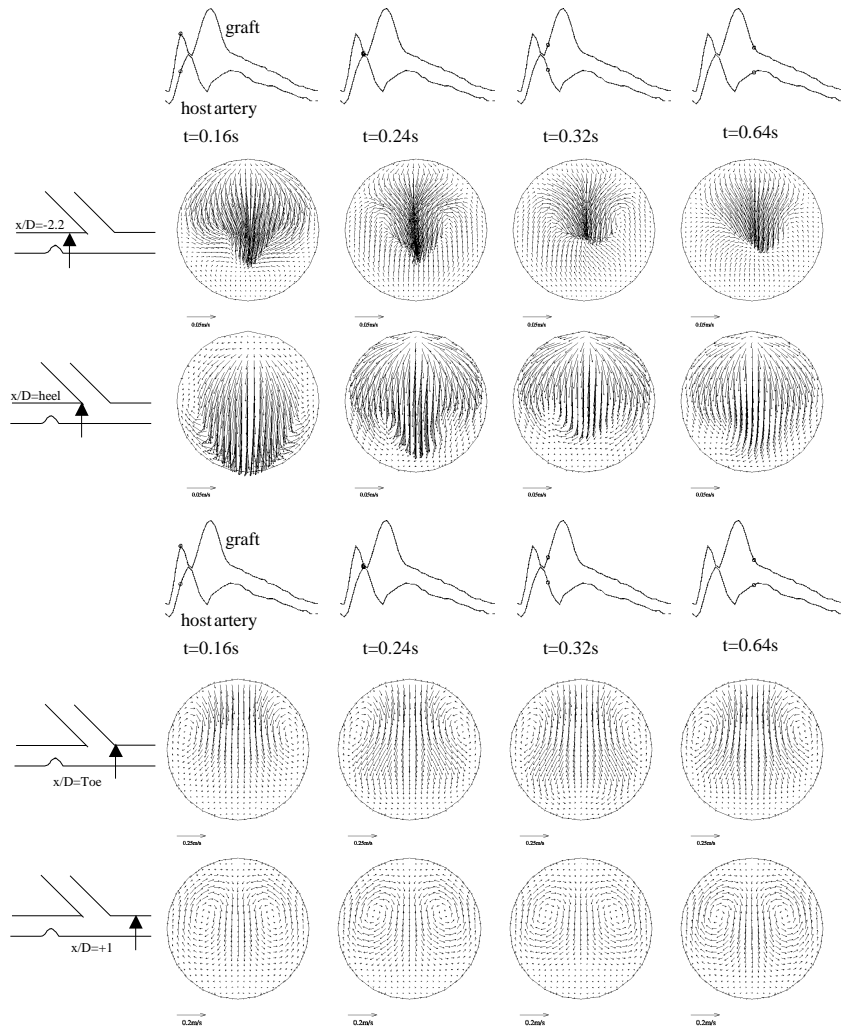


Figure 20: Secondary motions in  $yOz$  for 75% eccentric stenosis (2D-ec75PH2).

### 3.2.3 Distance of grafting

If several experimental and numerical studies have already demonstrated the potential beneficence of grafting with a minimal angle, the possibilities to improve the bypass surgical act in presence of residual flow are somewhat limited. If the intervention seems too risky for the graft viability (this point will be discussed in

§5), the surgical means to modify the situation are limited: either the surgery is not practised, or the graft is sutured more downstream if collateral arteries branches are sufficiently far, or on the contrary is sutured as close as possible to the stenosis.

Finally we have analyzed the effect of an increase in the distance of grafting onto the general hemodynamics in the coronary bypass. With a grafting distance of one diameter more than 2D-75PH2, the recirculation area can plainly develop but does not extends up to the heel during almost all the cycle except at  $t=0.32s$  (Figure 21). At this time, as for 2D-75PH2, the post-stenotic jet is deflected towards the bottom wall. Nevertheless, the flapping of the jet occurs but with a lesser amplitude. This is confirmed by the emission-lines (Figure 22) since with the longest distance of grafting (namely 3 diameters), the flow issued from the graft during deceleration, does not manage to notably deport the jet towards the bottom wall. The secondary motions in cross-sectional sections (not presented here) show also less disturbed velocity patterns especially at the heel.

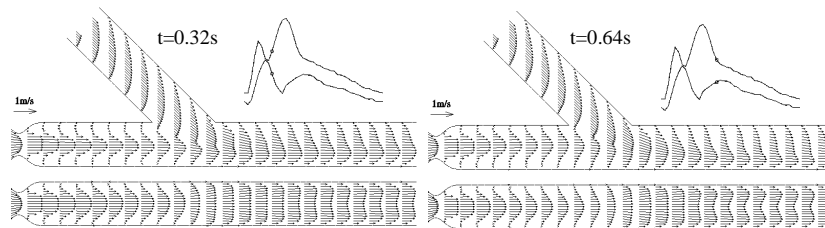


Figure 21: Longitudinal profiles for 3D-75PH2.

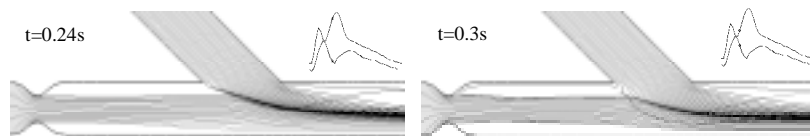


Figure 22: Emission lines with a longer distance of grafting 3D-75PH2.

### 3.3 Wall shear stress analysis

#### 3.3.1 Spatial distribution of the wall shear stress

The wss spatial distribution is presented for the most physiological flow rates, PH1 and PH2. In this latter case the two grafting length and the two shapes of the 75% stenosis (2D-75PH2 and 2D-ec75PH2) are presented. Among the sites prone to intimal hyperplasia –toe, heel, floor, suture line– the wss evolution is

plotted along the top wall from the stenosis to the heel (line A) and along the floor (line C) for different times. As a reference the mean and maximum Poiseuille infinite downstream values  $\tau_{mean}$  and  $\tau_{max}$  are calculated.

$$\tau_{mean} = \frac{32\mu Q_{mean}}{\pi D^3} \quad (7)$$

For the PH1 flow rate  $\tau_{mean}=25.9\text{dyn/cm}^2$  and  $\tau_{max}=26.9\text{dyn/cm}^2$ .

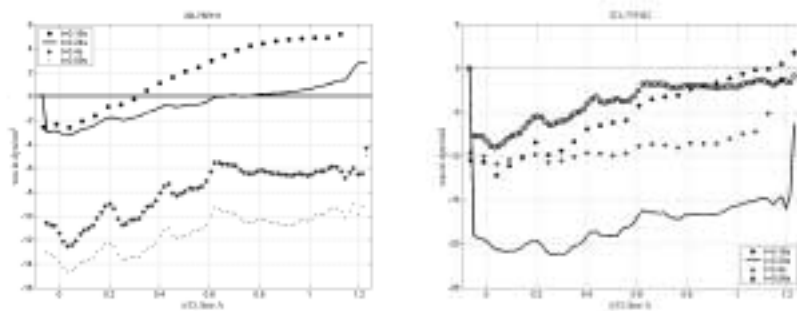
For the PH2 flow rate  $\tau_{mean}=46.3\text{dyn/cm}^2$  and  $\tau_{max}=52.3\text{dyn/cm}^2$ .

**3.3.1.1 Line A** (Figure 23) For the 2D-75PH1 case, the first systolic acceleration confines the recirculating area in the stenosis divergent. The wss values are therefore comprised between  $-3$  and  $+6\text{dyn/cm}^2$  and furthermore, positive in the vicinity of the heel. The recirculating area develops at the second and significative acceleration ( $t=0.4\text{s}$ ). Hence, the wss gets large negative values up to the heel and until the end of the cycle.

On the contrary, for the 2D-75PH2 case, the wss is immediately negative with the minimal value of about  $-22\text{dyn/cm}^2$  at  $t=0.32\text{s}$ . It remains negative up to the heel for the whole cycle.

Due to the jet confinement along the top wall the 2D-ec75PH2 wss values are positives, during the whole cycle. The wss value can reach, at the maximum of the graft flow rate, about 9,5 times bigger than its upstream infinite Poiseuille value. In addition, as the general evolution of the curves is a decreasing function following the velocity decrease along the top wall, we get low wss value at the heel.

Finally, for the 3D-75PH2 case, even if the wss is negative during few times in the cycle, since the second acceleration, the wss values are higher and often positive at the heel (approximately of  $+2$  to  $+6\text{dyn/cm}^2$ ) whereas negative for 2D-75PHY2.



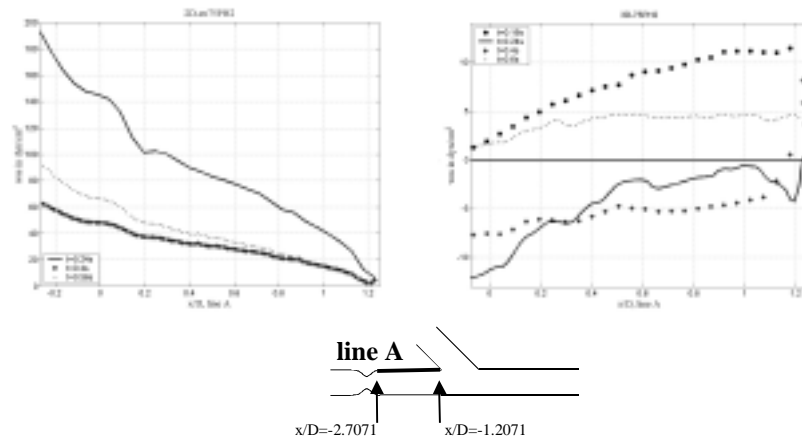
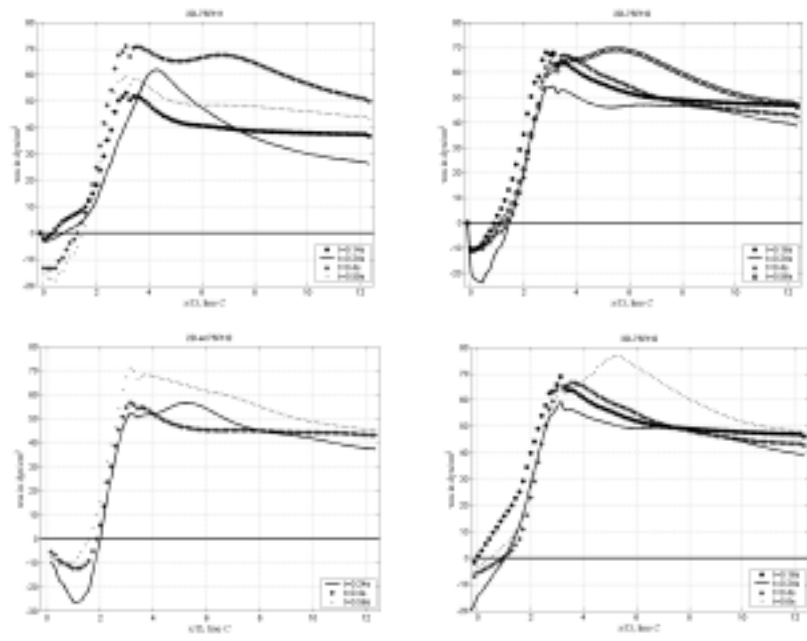


Figure 23: wss along line A.

**3.3.1.2 Line C** (Figure 24) Whatever the case the location of the reattachment point is time dependant. Its position follows the host artery flow rate variations with a small temporal dephasing. For the 2D-75PH1 case, its position varies from  $x/D=-2$  to  $x/D=-1.2$ . For the 2D-75PH2 case its position is more localized around  $x/D=1$  upstream from the junction unlike 3D-75PH2 case. The 2D-ec75PH2 case's recirculating area extension is more important than for the two others cases.

Distal to the junction, the position of the stagnation point (i.e. where the wss value is maximum) is also time dependant. The wss value can reach four times (for 3D-75PH2) the infinite wss value, submitting the coronary floor to high fluctuations on a short space.



**line C**  
 $x/D=-2.7071$                        $x/D=9$

Figure 24: wss along line C

### 3.3.2 wss variations on the skin

Figure 25 represents the variations, in  $N/m^2$ , of the x component of the wss on the skin of our model for 2D-75PH2 and 2D-84PH2 cases.

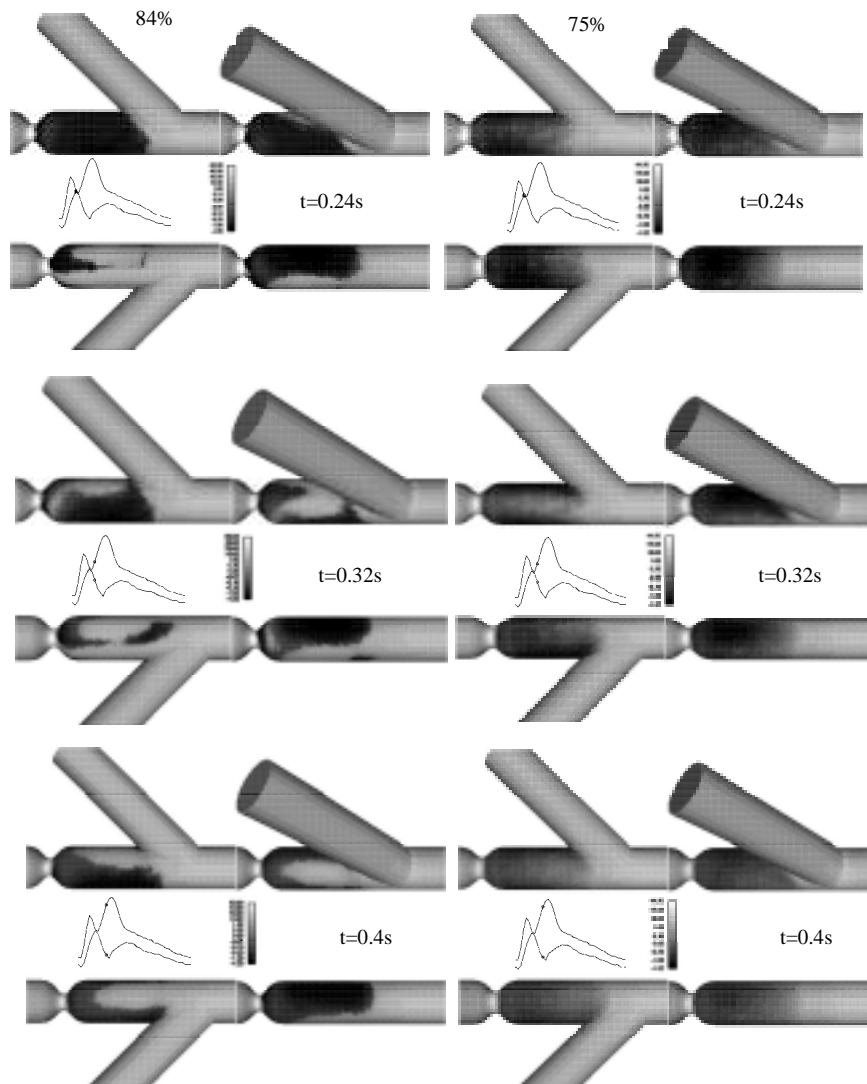


Figure 25: wss on the skin 2D-84PH2 (left) 2D-75PH2 (right).

According to section §3, the most severe stenosis implies higher wss values at the throat and lower wss values along the floor upstream to the junction. In addi-

tion, due to the strong jet deflection, the wss values are not uniformly distributed around the circumference. This phenomenon implies large spatial wss oscillations.

### 3.3.3 Temporal wss variations

The temporal wss variations are plotted (Figure 26) for the 2D-75PH2 case. Whatever the considered point, the general evolution follows the inflow waveform one. At the throat the wss values are the highest because of the jet effect, we get about 6.5 times bigger as the infinite Poiseuille value. Negative wss values are obtained at  $x/D=-1$  during the major part of the cycle. The sudden wss decrease represents the arrival of the vortex structure, induced by the recirculation, in the considered section. At  $x/D=\text{heel}$  on the floor the wss being nearly equal to  $-20\text{dyn/cm}^2$ , the artery works in “the opposite way” [43] of its upstream infinite behavior during almost the whole cycle: the early systolic acceleration and the diastole.

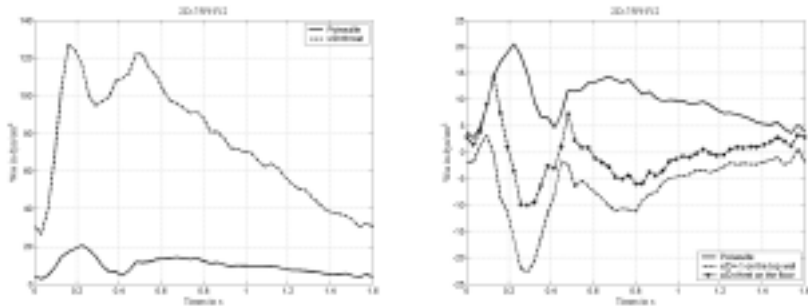


Figure 26: Temporal variation of wss.

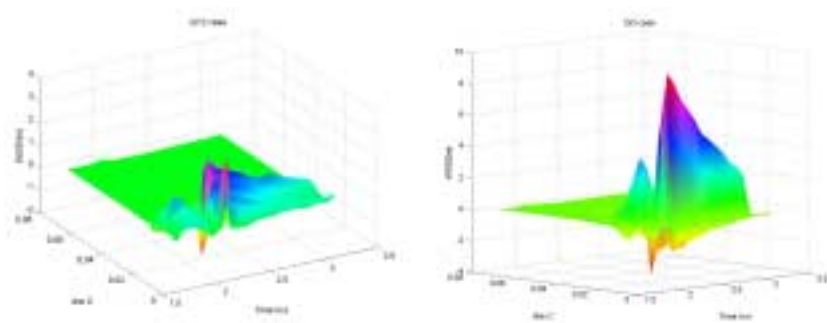


Figure 27: wss gradients.

### 3.3.4 Spatial wall shear stress gradients

Figure 23 presents the spatial wall shear stress gradients along the line C for two cases BLO and BL12. We define on this line the axial component of wss:  $\tau_x$  with:

$$\tau_x = \mu \left( \frac{\partial u}{\partial z} + \frac{\partial w}{\partial x} \right). \quad (8)$$

As many authors ([44], [45], [46]), the normalized spatial wall shear stress gradients,  $wssg_{nd}$ , is defined as:

$$wssg_{nd} = \frac{d\tau_x / dx}{\tau_{mean} / D}. \quad (9)$$

The stagnation point on the host artery floor is submitted to both high positive and negative  $wssg_{nd}$  values. For BL12 case these values can reach respectively up to 2.8 and  $-2$  at the maximum flow rate. For the BLO case, large values of  $wssg_{nd}$  appear in the upstream vicinity of the stagnation point. These values go up to 8.5 during the second deceleration.

## 3.4 Experimental validation

To validate our numerical computations, we compare Doppler experimental velocity envelopes (dotted line on Figure 28) for the 2D-75PH2 case with those numerically computed (plain line).

### 3.4.1 Comparison

The experimental model provides similar phenomena in the velocity fields: post-stenotic jet flow, deport of the maximum velocity towards anastomosis floor in xOz plane and double-peak velocity profiles in xOy plane. Nevertheless, several differences emerge especially beyond the stenosis.

In xOz plane, the experimental recirculation area appears ( $t=0.24s$ ), but less extended at top wall than at bottom wall. During the rest of the cycle, the jet is not markedly deflected in this plane.

In the other plane xOy, from  $t=0.24s$ , a great recirculating area is created at one of the lateral wall ( $y=+3mm$ ). The maximum jet velocity is at this time comprised in xOy, before skewing out of the measurement plane from  $t=0.32s$ . This deflection certainly explains the important velocity difference of 30-40% observed downstream from the stenosis. This error is only of 10% at the beginning of the flow graft deceleration (Figure 28,  $t=0.48s$ ) as well in xOz as in xOy.

On the other hand, experimental velocities measured downstream from the toe are in good agreement, qualitatively and quantitatively, with numerical ones. In early cycle, maximal u-velocities are very close in xOz. At  $x/D=2$  and  $t=0.56s$ , the peak u-component is more skewed towards the floor in numeric computations (located at  $y=+1.75mm$  versus  $+0.75mm$  in experiments).

In addition,  $xOy$  plane notifies non-symmetrical helical patterns initiated at  $t=0.24s$  and until  $t=0.56s$  i.e. during first stenosis flow deceleration. Influenced by the asymmetry of the jet, one of the helical structures is prevalent on the other one. This characteristic feature resembles to that observed numerically with a 84% stenosis. In this latter case (see §3.2.2), the jet deflection is visible in both planes. Consequently, in  $xOy$ , one of the helical structure is powerful than its twin. Finally, as preliminary tests under steady flow have exhibited the deflection towards the same wall, a slight manufacturing imperfection can lead to this major fluid-phenomenon.

To summarize, the velocity profiles encountered downstream from the anastomosis show a good agreement with those numerically computed. The average relative discrepancy is within 20%, which therefore enables the validation of our model.

#### **3.4.2 Limitations of the experiments**

Experimental model is made of a flexible material to diminish as much as possible the wave reflection that a rigid material as the Plexiglas could possibly induce. Anyway, with a maximal deformation of 17% (only 5% in the present work), Hofer et al. [47] have noticed a generally lower wss without significant changes in the hemodynamic patterns. But, one cannot not prevent a slight bending of the flexible bypass, which could imply supplementary instability. In fact, as further discussed in the text, any perturbation in the stenotic inflow or in the geometric shape can destabilize the perfect axi-symmetry of the post-stenotic jet.

Experimental velocity profiles are more rounded than numerical ones. As reported by [43], turbulence “in space” may appear at low Reynolds number, which therefore implies more dissipation and our laminar numerical model is, in one hand, somewhat limited to represent such critical flows. But on the other hand, the two experimental sample volumes do not exactly geometrically cross-check causing smoothing of the velocity profiles.

Besides, near-wall experimental velocities can also be overestimated because of ultrasonic beam reflection which is particularly marked at the furthest wall [48].

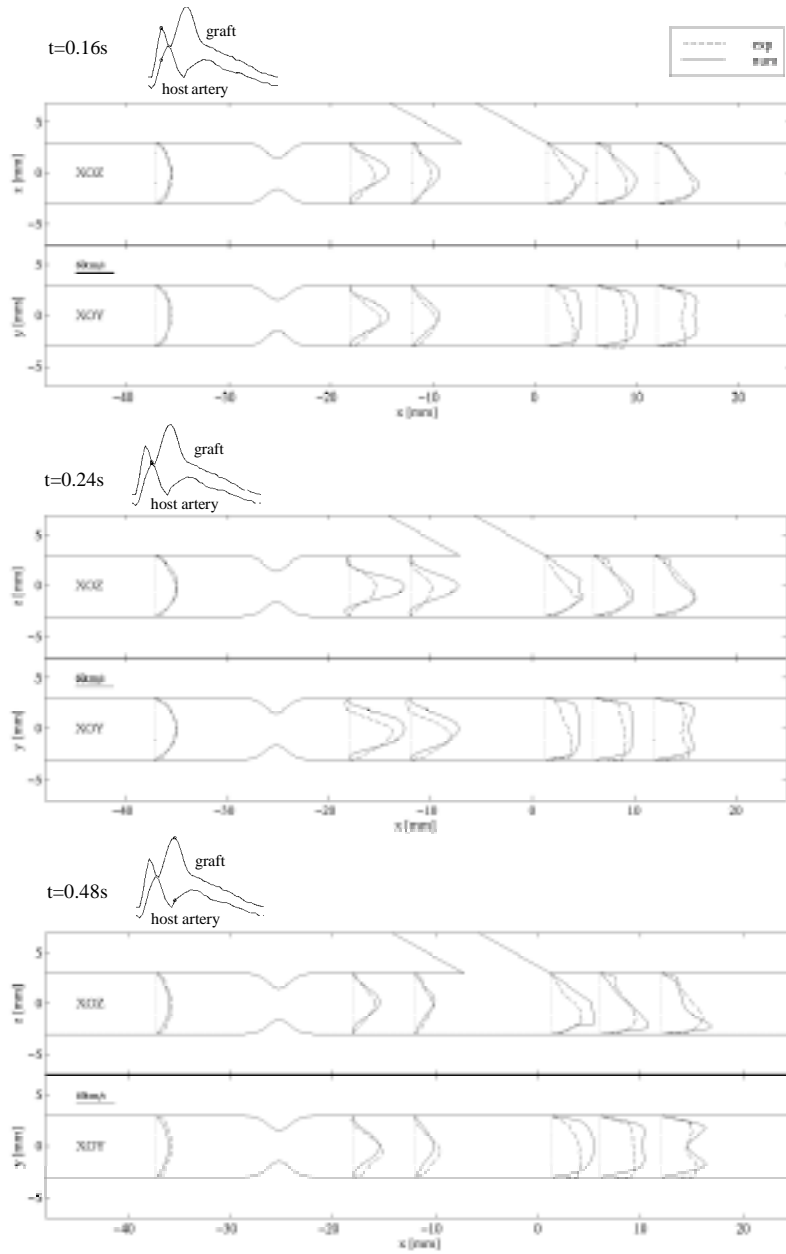


Figure 28: Experimental and numerical velocity profiles in  $xOz$  and  $xOy$  planes.

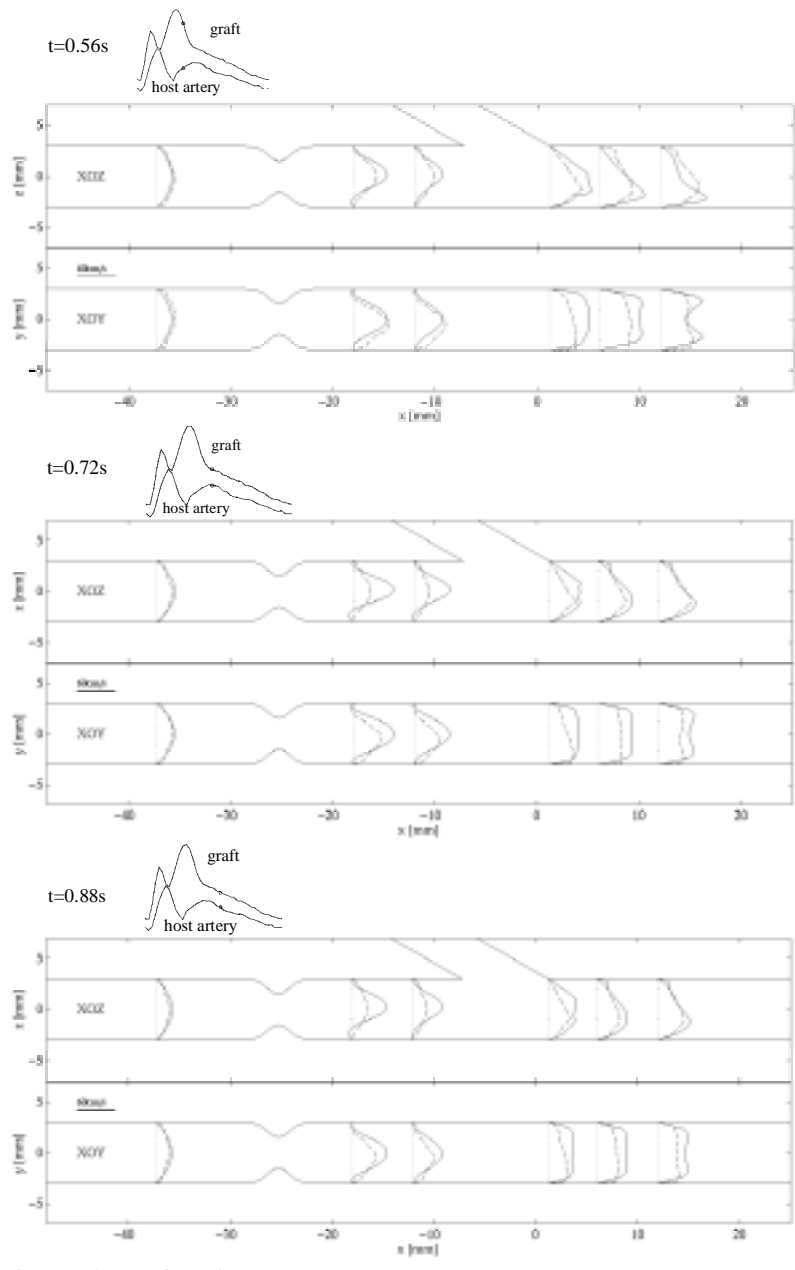


Figure 28: continued (reprinted from *J Biomech*, 34(8), Bertolotti et al. pp. 1049-1064, 2001, with permission of Elsevier Science).

## 4 Discussion upon hemodynamics patterns

The post-stenotic flows are known to be complex, three-dimensional and prone to become unstable, even at low Reynolds number. Therefore, the two recirculating zones emerging on both sides of a rectangular channel, may not keep a stable hydrodynamic configuration. In 2D channel just as through annular constriction, the separated flow is stable only when the pressure gradient is lower than a critical value [49]. Thus, a non-symmetrical flow can arise even if the geometry is symmetric (see also [50]). This phenomenon is sometimes referred as the Coanda effect [51]. Moreover, as experimentally observed by many authors, the deflection of the jet can originate from the interaction of a downstream phenomenon such as shear layer fluctuations, or oscillations of the reattachment point [49], [53], [54], [55], [56].

The strong jet deflection towards the top wall for the 2D-84PH2 case agrees with these experimental observations. In addition, as reported by [51], the asymmetry of the jet is not necessarily due to turbulence but rather to the flow instability imputable to small imperfections that are inevitable in any experimental apparatus. Such geometric imperfections can also come out from mesh realizations and give birth to dissymmetrical recirculation area. Tang et al. [50] who have also investigated jet deflection downstream from a 80% axi-symmetrical stenosis emphasize the necessity to perform three-dimensional models, even in numerical simulations, in order to truly represent the physical phenomena. 2D (axi-symmetrical) numerical problem often eliminate the potential for a jet to be dissymmetrical.

In addition to the jet deflection towards a "preferred" side, we can also observe its flapping in the 2D-75PH2 case. In our case the initiating factor of the flapping seems directly correlated with the dephased graft flow (see § 3.2.1.2). This assumption is corroborated by the fact that increasing the distance of grafting, and thus diminishing the perturbation upon the upstream flow, leads to a less pronounced flapping (see § 3.2.3). According to this unstable behavior, it is not really surprising to observe experimental deflection towards the lateral wall direction. Besides, without entering into further details on jet flows stability, our post-stenotic patterns are in good agreement with a lot of studies throughout literature.

This studies proves that these stenosis-induced fluid phenomena significantly alter the post-junction flow patterns. First, because jet influence propagates downstream from the junction, the counter-rotating secondary vortices are more confined to the top wall. The consequence is that the stasis zone which is tradi-

tionally reported at the toe, is eliminated ([30], [32]). Secondly, depending on the stenosis severity, four counter-rotating vortices, instead of only two, can be created, as merging flows in the vertebro-basilar confluence [40], [41]. In 2D-84PH2 case, an additional secondary vortex can evolve along the bottom wall of the distal anastomosis (see  $t=0.24s$ ,  $t=0.32s$ , Figure 17).

In conclusion, transient flows from typical human coronary bypasses conditions, have been numerically and experimentally studied. The flow fields have shown a major dependence on the inlet flows and on the stenosis shape. By analysing wss repartition, these investigated patterns could help to aim towards the least penalizing surgical configuration.

## 5 Clinical issues

The primary objective of the study was to examine how the post-operative residual flow interacts with the supplying flow issued from the graft to explain the restenosis process occurring at an early stage.

Among the mechanical-induced pathogenic factors, the wss is clearly identified as the main determinant of endothelial mechanotransduction [57]. By setting systemic risk agents that enhance thrombosis and cellular proliferation, the hemodynamic alteration of endothelial phenotype is believed to contribute to the focal progression of atherosclerosis. More precisely, elevated wss ( $>15\text{dyn/cm}^2$ ) is correlated with increased expression of endothelial nitric oxide synthase (eNOS) mRNA, and consequently of antiplatelet agents, fibrinolytics, and growth inhibitors [58]. This atheroprotective profile also renders the endothelium less susceptible to cell adhesion and lipid uptake. On the contrary, within a range of  $\pm 4\text{dyn/cm}^2$ , oscillatory (versus steady [10]) or turbulent [59] wss is a weaker inducer of eNOS, which is implicated in vascular tone and thus compensatory remodeling of arterial lumen. In fact, endothelial cells can stimulate the release of chemotactic factors and also mitogens that control migration and proliferation of cellular smooth muscles [60], [61], [62]. In this way, several authors ([63], [64], [6]) have identified low, negative and oscillating wss ( $-7$  to  $-0.5\text{dyn/cm}^2$ ) as the main hemodynamic feature involved in the outcome of the suture. In addition, Suter et al. [65] have found a significantly greater shear-induced platelet aggregation (40% at a stress amplitude of  $25\text{dyn/cm}^2$ ) in response to pulsatile (periodic stimuli within 0.7s) versus continuous shearing. The growth of the intramural thrombus is also been involved in the development of atherosclerotic plaques [60]. Furthermore, once activated by high shear stress at the stenosis throat, platelets and coagulation factors may be trapped into the recirculation area where they can interact with the injured wall [66], [67] because of an increased residence time and an augmented near-wall concentration [68], [69].

As a result of the interaction between jet flow –which can be dissymmetrical– and graft inflow, the first evidence is that, after surgery, the post-stenotic area wall is suddenly submitted to high spatial and temporal gradients of wss. These oscillations can dramatically vary with the out of phase of the two inflows and the severity of the stenosis. As an example, for 2D-75PH1, wss approximately ranges from  $-10$  to  $+10$  dyn/cm<sup>2</sup>, from  $-22$  to  $+12$  dyn/cm<sup>2</sup> for 2D-75PH2. The amplitude range goes down to  $-40$  dyn/cm<sup>2</sup> with a more severe stenosis of 84% (2D-84PH2) and the wss varies significantly more rapidly during the cycle. Nevertheless, with a longer distance of grafting like 3D-75PH2, the wss amplitudes are smoother and however, wss is almost always positive at the heel. In contrast, the occluded case predicts zero value upstream from the anastomosis and an overestimation of 40% of the wss peak at the distal anastomosis when comparing to case with residual flow BL34 (with a division ratio of 1/4 : 3/4 between recipient artery and graft).

All these results tend to prove that the heel and suture line are the most likely prone to intimal thickening in 2D-75PH2 compared to 2D-75PH1. Moreover, from our wss analysis, the area close to the stagnation point on the floor is submitted to large wss gradients. Elevated wss gradient values are expected to induce morphological modifications in endothelial layer that could imply the progression of atherosclerosis. As demonstrated by [70] with atomic force microscopy combined with numerical simulations, the disorganization of the endothelial surface results from high wss gradients. Cell responses may depend on the distribution of mechanosensors and the altered topography [57]. Moreover, local enhance in wall permeability is observed in these regions of high wss, that is generally related to atherogenesis [71]. These latter findings reinforce the affinity for 2D-75PH2 case to develop atherosclerosis compared to 2D-75PH1. Moreover, with a high grade stenosis (84%) the bottom wall could all the more preferentially be affected by the disease since large amplitudes of wss at the stagnation point are observed with an additional secondary structure that evolves at the same wall.

These investigations raise the badly understood problem of competitive flows. The distal narrowing is thought to be an adaptive response in diameter to competitive flow from the recipient artery [72]. Some theoretical studies [18], [73] [74], [75] have already examined such flows through simplistic 1D models. They put into evidence the existence of a critical value for stenosis severity, which depends on geometric features (diameters ratio, length of the arteries), and below which the failure of the graft is expected. Above this identified value, the recipient artery will tend to progressive occlusion. Of course, these models cannot predict 3D distribution of wss since the constriction is represented as a simple peripheral resistance, but they converge towards a valuable conclusion: increas-

ing distance of grafting amounts to diminish the downstream resistance seen by the flow that enters into the diseased artery. Another explanation for the subsequent failure of the graft is proposed. Our investigation 2D-75PH2 points out the perturbed flow patterns induced by a short distance of grafting and the potential benefit, in term of graft patency, to increase this distance if morphologic suitability for anastomosis is allowed.

On the other hand, the stasis area classically observed at the toe is considerably reduced when the distance of grafting is short. Furthermore, our present study tends to demonstrate that increasing the distance of grafting in case of severe or eccentric lesions, could boost the flapping of the jet. The following questions remain. Should the surgeon suture just beyond the stenosis to take advantage of the jet or on the contrary, bypass far from the jet influence to dissociate the combined effect of competitive flows from the healing of the suture line reported by Ballyk et al. [76]?

Recent clinical investigations tend to favor the second alternative. These authors [77] have revealed the higher risk of failure when bypassing low-grade stenosis. Problems of reobstruction have been specifically encountered with bypassed RCA, which could correspond to 2D-75PH2, 2D-84PH2 or 2D-ec75PH2 cases with high systolic velocity in our study. Stenoses of more than 60% in diameter (84% area) were also found to be a threshold for functioning from non functioning graft [78]. Internal thoracic artery grafts bypassed to mild stenosis were recently shown to narrow more easily [79]. With another graft configuration, Pagni et al. [80] suggest that grafting the IMA more distally may have a protective effect for the arterial graft because it would prevent the flow competition. Throughout our study, it seems difficult to predict the preferred side for jet deflection from the severity or the shape of the stenosis. Thus, increasing the distance of grafting with a more severe stenosis appears to be the most reasonable surgical solution to preserve the long-term graft flow.

Nevertheless, even if optimized configurations are theoretically highlighted in this exhaustive study, one must not forget that surgical act is somewhat limited by the anatomy, graft availability, suture technique, or histological state of the graft. And the simplicity of our geometric configurations does not allow extrapolating to definite conclusions. Current medical imaging such as magnetic resonance, scanner and stereo-angiography are able to furnish accurate geometrical data on the exact morphology of a healthy arterial segment [12], [13], [81]. Unfortunately, in vivo or in vitro evaluation of shape and velocity in the neighborhood of a localized atheroma plaque, remains unacceptably noisy [82], [83]. This explains the absence of studies including the realist geometry of a pathological narrowing especially in coronary artery disease.

Finally, several authors have reported that the success of the intervention does depend on the artery type. For example, the long-term results of coronary surgery for a 13-year period have shown 38% of graft failure for the saphenous vein and only 15–28% when the internal mammary arteries are used [84]. Another noticeable characteristic is that most of grafts are not interchangeable: the gastroepiploic artery is preferentially sutured onto RCA whereas internal thoracic artery rather on LAD [78], [85]. Thus, many questions still remain about the mechanical behavior of the arteries as well as their compliance matching. The mechanical behavior cannot be restricted to linearly elastic especially in atheroma, which is highly inhomogeneous, and anisotropic with an uncharacterized mechanical behavior. However, only animal experiments could help to resolve this uncertainty and the future modeling will have to progressively include the combination of all these realistic features with subject-specific pathologic information.

## References

- [1] Lawrie, G.M., Morris, G.C. & Earle, N. Long-term results of coronary bypass surgery. *Annals of Surgery*, **213**, pp. 377-385, 1991.
- [2] Hashimoto, H., Isshiki, T., Ikari, Y., Hara, K., Saeki, F., Tamura, T., Yamaguchi, T. & Suma, H. Effects of competitive blood flow on arterial graft patency and diameter. Medium-term postoperative follow-up. *Journal of Thoracic and Cardiovascular Surgery*, **111**, pp. 399-407, 1996.
- [3] Cosgrove, D.M., Loop, F.D., Saunders, C.L., Lytle, B.W. & Kramer, J.R., Should coronary arteries with less than fifty percent stenosis be bypassed? *Journal of Thoracic and Cardiovascular Surgery*, **82**, pp. 520-530, 1981.
- [4] Sottiurai, V. S., Yao, J. S. T., Batson, R. C., Sue, S. L., Jones, R. & Nakamura, Y. A. Distal anastomotic intimal hyperplasia: histopathological character and biogenesis. *Annals of Vascular Surgery*, **1**, pp. 26-33, 1989.
- [5] Sottiurai, V. S., Yao, J. S. T., Flinn, W. R., Batson, R. C. Intimal hyperplasia in neointima: an ultrastructural analysis of thrombosed grafts in humans. *Surgery*, **93**, pp. 809-817, 1983.
- [6] Zarins, C. K., Giddens, D. P., Bharadvaj, B. K., Sottiurai, V. S., Mabon, R. F. & Glagov, S. Carotid bifurcation atherosclerosis. Quantitative correlation of plaque localization with flow velocity profiles and wall shear stress. *Circulation Research*, **53**, pp. 502-514, 1983.
- [7] Malek, A.M., Alper, S.L. & Izumo, S. Hemodynamic shear stress and its role in atherosclerosis. *JAMA*, **282(21)**, pp. 2035-42, 1999.

- [8] Langille, B.L. & O'Donnell, F. Reductions in arterial diameter produced by chronic decreases in blood flow are endothelium-dependent. *Science*, **24**, **231(4736)**, pp. 405-7, 1986.
- [9] Kamiya, A. & Togawa, T. Adaptive regulation of wall shear stress to flow change in the canine carotid artery. *American Journal of Physiology*, **239(1)**, pp. H14-21, 1980.
- [10] Ziegler, T., Bouzourene, K., Harrison, V.J., Brunner, H.R. & Hayoz D. Influence of oscillatory and unidirectional flow environments on the expression of endothelin and nitric oxide synthase in cultured endothelial cells. *Arteriosclerosis Thrombosis and Vascular Biology*, **18(5)**, pp. 686-92, 1998.
- [11] Davies, P.F., Remuzzi, A., Gordon, E.J., Dewey, C.F. & Gimbrone, M.A. Turbulent fluid shear stress induces vascular endothelial cell turnover in vitro. *Proceedings of the National Academy of Science U S A*, **83(7)**, pp. 2114-7, 1986.
- [12] Zhao, S.Z., Xu, X.Y., Hughes, A.D., Thom, S.A., Stanton, A.V., Ariff, B. & Long, Q. Blood flow and vessel mechanics in a physiologically realistic model of a human carotid arterial bifurcation. *Journal of Biomechanics*, **33**, pp. 975-984, 2000.
- [13] Botnar, R., Rappitsch, G., Scheidegger, M.B., Liepsch, D., Perktold, K. & Boesiger, P. Hemodynamics in the carotid artery bifurcation: a comparison between numerical simulations and in vitro measurements. *Journal of Biomechanics*, **33**, pp. 137-144, 2000.
- [14] Cole, J.S., Gillan M.A., Raghunathan, S. & O'Reilly, M.J.G., Numerical simulations of time-dependent non Newtonian blood flow through typical human arterial bypass grafts. *6th Irish Chemical Engineering Research Symposium*, Cork, 1998.
- [15] Moore, J.A., Steinman, D.A., Prakash, S., Johnston, K.W., Ethier, C.R. & A numerical study of blood flow patterns in anatomically realistic and simplified end-to-side anastomoses. *Journal of Biomechanical Engineering* **121**, pp. 265-272, 1999.
- [16] Henry, F.S., Collins, M.W., Hughes, P.E. & How, T.V. Numerical investigation of steady flow in proximal and distal end-to-side anastomoses. *Journal of Biomechanical Engineering*, **118**, pp. 302-310, 1996.
- [17] Hughes, P. E. & How, T. V. Effects of geometry and flow division on flow structures in models of the distal end-to-side anastomosis. *Journal of Biomechanics*, **29**, pp. 855-872. 1996.
- [18] Furuse, A., Klopp, E. H., Brawley, R. K., Gott, V. L. Hemodynamics of aorta-to-coronary artery bypass. *Annals of Thoracic Surgery*, **14**, pp. 282-293, 1972. Back, L. H. Estimated mean flow resistance increase during

- coronary artery catheterization. *Journal of Biomechanics*, **27**, pp. 169–175, 1994.
- [19] Back, L. H. (1994) Estimated mean flow resistance increase during coronary artery catheterization. *Journal of Biomechanics*, **27**, 169-175.
- [20] Doucette, J.W., Corl, P.D., Payne, H.M., Flynn, A.E., Goto, M., Nassi, M. & Segal, J. Validation of a Doppler guide wire for intravascular measurement of coronary artery flow velocity. *Circulation*, **85**, pp. 1899–1911, 1992.
- [21] Bach, R. G., Kern, M. J., Donohue, T. J., Aguirre F. V. & Caracciolo, E. A. Comparison of phasic blood flow velocity characteristics of arterial and venous coronary artery bypass conduits. *Circulation*, **88**, pp. 133-140, 1993.
- [22] Berne, R. M. & Levy, M. N. *Cardiovascular Physiology*. Mosby: St. Louis, MO, pp. 201, 1967.
- [23] Womersley, J.R. Method for the calculation of velocity, rate of flow and viscous drag in arteries when the pressure gradient is known. *Journal of Physiology*, **127**, pp. 553–563, 1955.
- [24] N3S, Electricité De France©, Simulog, 1 rue James Joule, 78286 Guyancourt cedex, France.
- [25] Bertolotti C. & Deplano V. Three-dimensional numerical simulations of flow through a stenosed coronary bypass. *Journal of Biomechanics*, **33(8)**, pp.1011-22, 2000.
- [26] Gach, H.M. & Lowe, I.J. Characterization of flow emerging from a stenosis using MRI. *Magnetic Resonance in Medicine*, **40(4)**, pp. 559-570, 1998
- [27] Ghalichi, F., Deng, X., De Champlain, A., Douville, Y., King, M. & Guidoin, R. Low Reynolds number turbulence modeling of blood flow in arterial stenoses. *Biorheology*, **35**, pp. 281-294, 1998
- [28] Bluestein, D., Gutierrez, C., Londono, M. & Schoepfoerster, R.T. Vortex shedding in steady flow through a model of an arterial stenosis and its relevance to mural platelet deposition. *Annals of Biomedical Engineering*, **27**, pp. 763-773, 1999.
- [29] Chorin, A. J. Numerical solution of the Navier-Stokes equations. *Math. Comput.*, **22**, pp. 745-762, 1968.
- [30] Hughes, P. E. & How, T. V. Effects of geometry and flow division on flow structures in models of the distal end-to-side anastomosis. *Journal of Biomechanics*, **29**, pp. 855-872, 1996.
- [31] White, S. S., Zarins, C. K., Giddens, D. P., Bassiouny, H., Loth, F., Jones, S. A. & Glagov, S. Hemodynamics patterns in two models of end-to-side vascular graft anastomoses: effects of pulsability, flow division, reynolds

- number, and hood length. *Journal of Biomechanical Engineering*, **115**, pp. 104-111, 1993.
- [32] Inzoli, F., Migliavacca, F. & Pennati, G. Numerical analysis of steady flow in aorto-coronary bypass 3-D model. *Journal of Biomechanical Engineering*, **118**, pp. 172-179, 1996.
- [33] Ojha, M., Ethier, R. C., Johnston, W. K., & Cobbold, R. S. C. Steady and pulsatile flow fields in an end-to-side arterial anastomosis model. *Journal of Vascular Surgery*, **12**, pp. 747-753, 1990.
- [34] Keynton, R. S., Rittgers, S. E. & Shu, M. C. The effect of angle and flow rate upon hemodynamics in distal vascular graft anastomoses: an in vitro model study. *Journal of Biomechanical Engineering*, **113**, pp. 458-463, 1991.
- [35] Siouffi, M., Deplano, V. & Pélissier, R. Experimental analysis of unsteady flows through a stenosis. *Journal of Biomechanics*, **31**, pp. 11-19, 1998.
- [36] Ojha, M., Cobbold, R. S. C., Johnston, K. W. & Hummel, R. L. Pulsatile flow through constricted tubes: an experimental investigation using photochromic tracer methods. *Journal of Fluid Mechanics*, **203**, pp. 173-197, 1989.
- [37] Widnall, S. E. & Sullivan, J. P., On the stability of vortex rings. *Proceedings of the Royal Society of London*, **A. 332**, pp. 335-353, 1973.
- [38] Siouffi-Freyder, M. Analyse des effets instationnaires sur les caractéristiques de l'écoulement en aval d'un rétrécissement local de section. *Doctorat de 3<sup>e</sup> cycle*, Université d'Aix – Marseille II, 1988.
- [39] Stroud J.S., Berger S.A., Saloner D. Influence of stenosis morphology on flow through severely stenotic vessels : implications for plaque rupture. *Journal of Biomechanics*, **33**, pp. 443-455, 2000.
- [40] Ravensbergen, J., Krijger, J. K. B., Hillen, B. & Hoogstraten, H. W. , Merging flows in an arterial confluence: the vertebro-basilar junction. *Journal of Fluid Mechanics*, **304**, pp. 119-141, 1995.
- [41] Ravensbergen, J., Ravensbergen, J. W., Krijger, J. K. B., Hillen, B. & Hoogstraten, H. W., Localizing role of hemodynamics in atherosclerosis in several human vertebrobasilar junction geometries. *Arterioscler. Thromb. Vasc. Biol.* **18**, pp. 708-716, 1998.
- [42] Ojha, M., Leask, R.L., Butany, J. & Johnston, K.W. Distribution of intimal and medial thickening in the human right coronary artery: a study of 17 RCAs. *Atherosclerosis*, **158(1)**, pp. 147-53, 2001.
- [43] Deplano, V. & Siouffi, M. Experimental and numerical study of pulsatile flows through stenosis: wall shear stress analysis. *Journal of Biomechanics* **32**, pp. 1081-1090, 1999.

- [44] Kleinstreuer, C., Lei M. & Buchanan J., Archie J. Hemodynamics of a femoral graft-artery connector mitigating restenosis. *Proceedings of the 1995 Bioengineering Conference*, eds. Hull, M. ASME Press, New York, BED -vol. **31**, pp. 171-172, 1995.
- [45] Lei M, Kleinstreuer, C. & Truskey G. Numerical analysis and prediction of atherogenic sites in branching arteries. *ASME Journal of Biomechanical Engineering*, **117**, pp. 350-357, 1995.
- [46] Ethier, C.R., Steinman, D.A., Zhang, X., Karpik, S.R. & Ojha, M. Flow waveform effects on end to side anastomotic flow patterns. *Journal of Biomechanics*, **31**, pp. 609-617, 1998.
- [47] Hofer, M., Rappitsch, G., Perktold, K., Trubel, W. & Schima, H. Numerical study of wall mechanics and fluid dynamics in end-to-side anastomoses and correlation to intimal hyperplasia. *Journal of Biomechanics*, **29**, pp. 1297-1308. 1996.
- [48] Bossuet, P. Simulation in vitro de la macrocirculation cérébrale en pathologie carotidienne – Comparaison aux données de la simulation numérique. PhD Thesis, Institut National Polytechnique de Toulouse, France. 1997.
- [49] Borgas M.S. & Pedley T.J. Non-uniqueness and bifurcation in annular and planar channels flows. *Journal of Fluid Mechanics*, **214**, pp. 229-250, 1990.
- [50] Tang D., Yang C. & Ku D.N. A 3-D thin-wall model with fluid-structure interactions for blood flow in carotid arteries with symmetric and asymmetric stenoses. *Computers & Structures*, **72**, pp. 357-377, 1999.
- [51] Fearn, R.M., Mullin, T. & Cliffe, K.A. Nonlinear flow phenomena in a symmetric sudden expansion. *Journal of Fluid Mechanics*, **211**, pp. 595-608, 1990.
- [52] Pagneux, V. & Maurel, A. A numerical study of instabilities in confined open flows. *Comptes Rendus de l'Académie des Sciences Série II-Mécanique Physique Chimie Sciences de la Terre et de l'Univers*, **319 (6 Part 1)**, pp. 617-623. 1994.
- [53] Iribarne, A., Frantisak, F., Hummel, R.L. & Smith, J.W. An experimental study of instabilities and other flow properties of a laminar pipe jet. *AIChE Journal*, **18**, pp. 689-698. 1972.
- [54] Latornell, D.J. & Pollard, A. Some observations on the evolution of shear layer instabilities in laminar flow through axisymmetric sudden expansion. *Physics of Fluids*, **29**, pp. 2828-2835. 1986.
- [55] Sobey, I.J. Observations of waves during oscillatory channel flow. *Journal of Fluid Mechanics*, **151**, pp. 395-426. 1985.
- [56] Sreenivasan, K. R. & Strykowski, P. J. An instability associated with a sudden expansion in a pipe flow. *Physic of Fluids*, **26**, 2766-2768, 1983.

- [57] Davies, P.F., Barbee, K.A., Volin, M.V., Robotewskyj, A., Chen, J., Joseph, L., Griem, M.L., Wernick, M.N., Jacobs, E., Polacek, D.C., dePaola, N. & Barakat, A.I. Spatial relationships in early signaling events of flow-mediated endothelial mechanotransduction. *Annual Reviews of Physiology*, **59**, pp. 527-49, 1997.
- [58] Mattsson EJ, Kohler TR, Vergel SM, Clowes AW. Increased blood flow induces regression of intimal hyperplasia. *Arterioscler Thromb Vasc Biol*. **17(10)**, pp. 2245-9, 1997.
- [59] DePaola, N., Gimbrone, M.A. Jr, Davies, P.F. & Dewey, C.F. Jr. Vascular endothelium responds to fluid shear stress. *Arteriosclerosis and Thrombosis*. **12(11)**, pp. 1254-7, 1992.
- [60] Ross, R., The pathogenesis of atherosclerosis – an update. *New England Journal of Medicine*, **314**, pp. 488-501, 1986.
- [61] Ross, R. The pathogenesis of atherosclerosis: a perspective for the 1990s. *Nature*, **362**, pp. 801-809, 1993.
- [62] Ross, R. Atherosclerosis: an inflammatory disease. *N Engl J Med*, **340**, pp. 115-126, 1999.
- [63] Ku, D. N, Zarins, C. K., Giddens, D. P. & Glagov, S. Pulsatile flow and arteriosclerosis in the human carotid bifurcation: positive correlation between plaque localization and low and oscillating shear stress. *Arteriosclerosis*, **5**, pp. 292-302, 1985.
- [64] Bassiouny, H. S., White, S., Glagov, S., Choi, E., Giddens, D. P. & Zarins, K. Anatomic intimal hyperplasia: mechanical injury or flow induced. *Journal of Vascular Surgery*, **15**, pp. 708-717, 1992.
- [65] Sutera, S.P., Nowak, M.D., Joist, J.H., Zeffren, D.J. & Bauman, J.E. A programmable, computer-controlled cone-plate viscometer for the application of pulsatile shear stress to platelet suspensions. *Biorheology*, **25**, pp. 449-459, 1988.
- [66] Badimon, L., Badimon, J. J., Galvez, A., Chesebro, J. H. & Fuster, V. Influence of arterial damage and wall shear stress rate on platelet deposition; Ex vivo study in a swine model. *Arteriosclerosis*, **6**, pp. 312, 1986.
- [67] Reininger, A. J., Reininger, C. B., Heinzmann, U., & Wurzing, L. J. Residence time in niches of stagnant flow determines fibrin clot formation in an arterial branching model - detailed flow analysis and experimental results. *Thrombosis Haemostasis*, **74**, pp. 916-922, 1994.
- [68] Goldsmith, H.L. & Turitto, V.T. Rheological aspects of thrombosis and haemostasis: basic principles and applications. *Thrombosis Haemostasis*, **55**, pp. 415-435. 1986.
- [69] Aarts, P. A., Van Den Broek, S. A., Prins, G. W., Kuiken, G. D., Sixma, J. J. & Heethaar, R. M. Blood platelets are concentrated near the wall and red

- blood cells, in the center in flowing blood. *Arteriosclerosis*, **8**, pp. 819-824, 1988.
- [70] Barbee, K.A., Mundel, T., Lal, R. & Davies, P.F. Subcellular distribution of shear stress at the surface of flow-aligned and nonaligned endothelial monolayers. *American Journal of Physiology*, **268(4 Pt 2)**, pp. H1765-72, 1995.
- [71] Buchanan, J.R. Jr, Kleinstreuer, C., Truskey, G.A. & Lei M. Relation between non-uniform hemodynamics and sites of altered permeability and lesion growth at the rabbit aorto-celiac junction. *Atherosclerosis*, **143(1)**, pp. 27-40. 1999.
- [72] Geha, A.S., Krone, R.J., McCormick, J.R. & Baue, A.E. Selection of coronary bypass. Anatomic, physiological, and angiographic considerations of vein and mammary artery grafts. *Journal of Thoracic Cardiovascular Surgery*, **70(3)**, pp. 414-31, 1975.
- [73] Einav, S., Avidor, J., & Vidne, B. Haemodynamics of coronary artery – saphenous vein bypass. *Journal of Biomechanical Engineering*, **7**, pp. 305-309, 1985.
- [74] Wiesner, T.F., Levesque, M.J., Rooz, E. & Nerem, R.M. Epicardial coronary blood flow including the presence of stenoses and aorto-coronary bypasses-II: Experimental comparison and parametric investigations. *Journal of Biomechanical Engineering*, **110**, pp. 144-149, 1988.
- [75] Yasuura, K., Takagi, Y., Ohara, Y., Takami, Y., Matsuura, A. & Okamoto, H. Theoretical analysis of right gastroepiploic artery grafting to right coronary artery. *Annals of Thoracic Surgery*, **69**, pp. 728-731. 2000.
- [76] Ballyk, P.D., Walsh, C., Butany, J. & Ojha, M. Compliance mismatch may promote graft-artery intimal hyperplasia by altering suture-line stresses. *Journal of Biomechanics*, **31**, pp. 229-237, 1998.
- [77] Buxton, B.F., Ruengsakulrach, P., Fuller, J., Rosalion, A., Reid, & C.M., Tatoulis, J. The right internal thoracic artery graft - benefits of grafting the left coronary system and native vessels with a high grade stenosis. *European Journal of Cardiothoracic Surgery*, **18**, pp. 255-261, 2000.
- [78] Hashimoto, H., Isshiki, T., Ikari, Y., Hara, K., Saeki, F., Tamura, T., Yamaguchi, T. & Suma, H. Effects of competitive blood flow on arterial graft patency and diameter. Medium-term postoperative follow-up. *J Thorac Cardiovasc Surg*, **111(2)**, pp. 399-407, 1996.
- [79] Hirotsu, T., Kameda, T., Shirota, S. & Nakao, Y. An evaluation of the intraoperative transit time measurements of coronary bypass flow. *Eur J Cardiothorac Surg.* **19(6)**, pp. 848-52, 2001.
- [80] Pagni, S., Storey, J., Ballen, J., Montgomery, W., Qaqish, N.K., Etoch, S. & Spence, P.A. Factors affecting internal mammary artery graft survival:

how is competitive flow from a patent native coronary vessel a risk factor?  
*Journal of Surgical Research*, **71**, pp. 172-178, 1997.

- [81] Long, Q., Xu, X.Y., Bourne, M. & Griffith, T.M. Numerical study of blood flow in an anatomically realistic aorto-iliac bifurcation generated by MRI data. *Magnetic Resonance in Medicine*, **43**, pp. 565-576, 2000.
- [82] Cloutier, G., Qin, Z., Garcia, D., Soulez, G., Oliva, V. & Durand, L.G. Assessment of arterial stenosis in a flow model with power Doppler angiography: accuracy and observations on blood echogenicity. *Ultrasound in Medicine and Biology*, **26(9)**, pp. 1489-501, 2000.
- [83] Pennell, D.J., Bogren, H.G., Keegan, J., Firmin, D.N., Underwood, S.R., Assessment of coronary artery stenosis by magnetic resonance imaging. *Heart*, **75**, pp. 127-133, 1996.
- [84] Cameron, A., Kemp, H.G. Jr & Green, G.E. Internal mammary artery grafts, fifteen years follow up. *Abstracts of the 58th Scientific Sessions of the American Heart Association, Circulation, Part II 72 supp. III(4)*, pp. 293, 1985.
- [85] Hamada, Y., Kawachi, K., Yamamoto, T., Nakata, T., Kashu, Y., Watanabe, Y. & Sato, M. Effect of coronary artery bypass grafting on native coronary artery stenosis. Comparison of internal thoracic artery and saphenous vein grafts. *J Cardiovasc Surg (Torino)*, **42(2)**, pp. 159-64, 2001.